



Research Papers

Thermoelectric materials based on cobalt-containing sintered silicon-germanium alloys

Nikita Grevtsov^{a,*}, Eugene Chubenko^a, Vitaly Bondarenko^a, Ilya Gavrilin^b, Alexey Dronov^b, Sergey Gavrilov^b, Dmitry Goroshko^c, Olga Goroshko^c, Grigory Rymyski^d, Kazimir Yanushkevich^d

^a Belarusian State University of Informatics and Radioelectronics, Minsk, Belarus

^b National Research University of Electronic Technology, Zelenograd, Moscow, Russia

^c Institute of Automation and Control Processes, Far Eastern Branch, Russian Academy of Sciences, Vladivostok, Russia

^d Scientific-Practical Materials Research Centre of NAS of Belarus, Minsk, Belarus



ARTICLE INFO

Keywords:

Electrochemical deposition
Semiconductors
Silicon-germanium
Cobalt
Cobalt silicides
Thermoelectric materials

ABSTRACT

Thermoelectric materials based on cobalt-containing SiGe alloy films were fabricated using monocrystalline silicon wafers with thin porous silicon layers electrochemically decorated with cobalt nanoparticles, filled germanium and subsequently subjected to rapid thermal processing. SEM, XRD, Raman spectroscopy and measurements of electrical conductivity and thermoelectric parameters revealed that an intermediate silicidation step involving thermal processing at 850 °C after cobalt deposition is crucial to maximize the resulting alloy's thermoelectric capabilities. The obtained silicidized SiGe:Co samples demonstrate a Seebeck coefficient of -450 μV/K and an estimated figure-of-merit ZT value of up to 0.72 at 450 K due to the presence of crystalline cobalt silicides in the film. These results enable a new approach to the fabrication of thin film thermoelectric materials based on SiGe alloys.

1. Introduction

The need for the development of highly efficient thermoelectric converters cannot be overemphasized, since about 90 % of the world's energy consumption today is associated with the generation or conversion of heat, of which about 60 % is considered waste heat [1]. Energy harvesting is an important concept for reducing energy waste in both industrial and domestic circumstances [2,3].

Performance of thermoelectric materials is reliant on possessing low thermal conductivity and electrical resistivity and is characterized by the dimensionless figure-of-merit ZT , defined as $ZT = (S^2/\rho\kappa)T$, where S is the Seebeck coefficient, ρ is the electrical resistivity, κ is the thermal conductivity and T is the absolute temperature. Currently, the best experimental values of $ZT > 2$ were achieved at room temperature in laboratory conditions in materials containing rare (SnSe) or toxic (PbTe) substances [2,4,5]. The more commonly used silicon-germanium ($\text{Si}_{1-x}\text{Ge}_x$, SiGe) alloys are considered to be among the most reliable high-temperature thermoelectric materials, having already proven themselves in both terrestrial and extraterrestrial applications [2,6].

They are praised for their abundance, non-toxicity, ease of n- and p-type doping and high efficiency at temperatures above 600 °C [6–8]. However, bulk SiGe's efficiency at lower temperatures is not quite as impressive compared to other known thermoelectric materials such as Bi_2Te_3 , Bi_2Se_3 , FeSi_2 and BiSb , which boast superior Seebeck coefficient and ZT values [9–11]. To improve SiGe's performance, various approaches can be undertaken. One such approach involves optimizing the ratio of silicon and germanium contents in the alloy. In research dating back to 1968 [12] it was concluded that, despite the maximum Seebeck coefficient achieved at $x = 0.15$, an optimal alloy composition lies closer to $\text{Si}_{0.7}\text{Ge}_{0.3}$, since its thermal conductivity at 300–900 K remains at its minimum [13]. In a silicon-enriched alloy the solubility limit of n-type dopants is higher, enabling an increase in carrier concentration, as well as an additional reduction in thermal conductivity due to intense electron-phonon scattering. The melting points and band gaps of these alloys are also sufficient, making them favorable for use in high-temperature conditions.

Improving thermoelectric efficiency by increasing the power factor and simultaneously reducing thermal conductivity is far from a trivial

* Corresponding author.

E-mail address: hrautsou@gmail.com (N. Grevtsov).

<https://doi.org/10.1016/j.matresbull.2024.113258>

Received 23 August 2024; Received in revised form 6 November 2024; Accepted 8 December 2024

Available online 9 December 2024

0025-5408/© 2024 Elsevier Ltd. All rights reserved, including those for text and data mining, AI training, and similar technologies.

task. In thermoelectric materials the major heat carriers are electrons and phonons — their contributions towards a given material's overall thermal conductivity are known as electronic thermal conductivity and lattice thermal conductivity, respectively [14]. The latter is normally the dominant contributor in elemental semiconductors; however, this changes in alloys, where the input of lattice thermal conductivity is significantly reduced due to mass fluctuation causing an increase in phonon scattering [15,16]. Even further reduction would require taking into account and maximizing the various scattering mechanisms occurring during phonon transport. For heavily-doped thermoelectric materials such as the SiGe alloys in question, that would include phonon-phonon and electron-phonon scattering [17].

Recent advances in the field of SiGe-based thermoelectrics suggest that another effective strategy towards decreasing thermal conductivity is nanostructuring [18]. The primary reason for this is the fact that the average mean free path of phonons is longer than that of electrons, so the formation of additional scattering regions by any means (such as creation of interfaces or free surfaces) will more actively suppress thermal conductivity than reduce electrical conductivity. It is desirable to form not only nanoscale regions (3–100 nm) for effective scattering of short- and medium-wavelength phonons, but also larger ones (0.1–1 μm , such as grain boundaries) for scattering of long-wavelength phonons [19]. In addition to the reduction in thermal conductivity, the power factor can also be improved in nanostructured or composite materials due to the so-called energy filtering effect, wherein the Seebeck coefficient is significantly increased due to a strongly energy-dependent electron scattering rate [20].

Theoretical calculations conducted for nanostructured SiGe [21] and a nanocomposite comprised of both metallic and semiconducting silicides [22] have shown the latter to exhibit higher ZT values at 300–900 K due to reduced thermal conductivity compared to pristine SiGe. This has been experimentally confirmed [23] for a SiGe nanocomposite based on FeSi_2 and Mg_2Si — two semiconducting silicides characterized by good thermoelectric properties [24], as well as some other narrow-gap silicides including CrSi_2 [25], MoSi_2 [26] and WSi_2 [27].

For the formation of SiGe nanocomposites, it is possible to go beyond semiconductor silicides. Some works [28,29] have shown that a two-phase heterostructure consisting of an efficient thermoelectric material and a benign metal with high electrical and thermal conductivity constitutes an optimal thermoelectric composite. This concept has been experimentally confirmed in [30], where well-dispersed metallic YSi_2 nano-inclusions forming coherent nanoscale boundaries with a p-type SiGe matrix have demonstrated a drastic reduction in thermal conductivity without compromising the power factor.

One of the most notable metallic silicides is CoSi_2 . A silicon nanocomposite structure with sub-micron CoSi_2 inclusions was shown to exhibit a 16 % increase in ZT compared to a bulk Si composite consisting of sub-micron SiB_3 precipitates [31]. According to the authors, this result was achieved due to the reduction in thermal conductivity through enhanced phonon scattering on the precipitate/matrix interfaces, which is in agreement with the arguments presented above. The Si/ CoSi_2 composite's electrical performance was retained due to the similarity in crystal structures (cubic diamond for Si and cubic fluorite for CoSi_2) and lattice parameters (mismatch within 1.2 % at room temperature), which reduced the density of interfacial dislocations. According to Vegard's law, the lattice mismatch between a SiGe alloy with Ge contents of 30 % and CoSi_2 would be about 2.4 %, enabling the latter's epitaxial formation on the former [32].

In order to form a composite thermoelectric material based on CoSi_2 and SiGe, it is important to maintain the phase composition during temperature change. It is known that Co can form compounds with germanium [33], but the large difference in the heat of formation between CoSi_2 (-102.9 kJ/mol [34]) and CoGe_2 (-17.4 kJ/mol [35]) favors the former process. As such, in a ternary compound consisting of silicon, germanium and cobalt, two phases should predominantly form: the SiGe alloy and cobalt disilicide.

Porous silicon (PS) possesses a variety of unique characteristics that make it well-suited for application in integrated devices such as light-emitting diodes and optical waveguides [36,37], but is also widely regarded as a prominent candidate for use as a structural matrix for a variety of composite materials [38,39]. Recently we have developed a new approach to fabricating SiGe films based on PS matrices formed by electrochemical anodization that involves electrochemically filling pores with germanium and subjecting the as-prepared composite to rapid thermal processing (RTP) [40]. The proposed method is simple and suitable for cheap mass production of SiGe alloys. It was successfully employed to produce n -type (phosphorous or antimony doped) and p -type (boron doped) materials, with the doping type and level determined by those of the initial silicon wafer. A high demand for the development of low cost and high efficiency thermoelectric materials motivated us to also investigate SiGe– CoSi_2 nanocomposites, since our method allows the introduction of cobalt into the alloy at the preparatory stage. The present work aims to further evaluate the specifics of nanocomposite formation using this proposed method, as well as study the resulting materials' thermoelectric characteristics.

2. Materials and methods

2.1. Processing

Fig. 1 illustrates the samples' production stages, taking into account the corresponding structure analysis results, which will be presented and discussed further. Three types of samples were fabricated and studied in this work. In each case, the initial porous matrix consisted of PS formed by electrochemical anodization.

For the first sample type, germanium was electrochemically deposited into the as-grown porous layer, followed by rapid thermal processing (RTP 2) for alloying. The process in question was previously described in detail [40], and the result is sufficiently reproducible; as such, this sample type was used as a reference for the other two and will be subsequently referred to as reference SiGe. The fabrication of the second sample type additionally included electrochemical deposition of cobalt into the initial PS layer using an aqueous solution of CoSO_4 . It was assumed that subsequent germanium deposition and RTP 2 would lead to the simultaneous formation of silicon-germanium alloys and cobalt silicides, with the latter serving as additives in the SiGe alloy, improving its thermoelectric characteristics. This sample type will be referred to as unsilicidized SiGe:Co. Lastly, for the third type of samples, an additional RTP stage (RTP 1) was introduced after cobalt deposition for preliminary cobalt silicide formation — these samples will be referred to as silicidized SiGe:Co.

Electrochemical anodization, as well as cobalt and germanium deposition processes were carried out in a PTFE electrochemical cell, with a horizontally oriented working electrode (silicon wafer) located at the bottom part of the cell. A platinum wire served as a counter-electrode. A Metrohm Autolab PGSTAT302N potentiostat/galvanostat was used to set up the necessary electrical processing regimes.

PS layers were formed on highly antimony-doped (0.01 Ohm-cm) monocrystalline n^+ -type silicon wafers with (100) crystallographic orientation. Electrochemical anodization was carried out at 70 mA/cm² in a solution containing hydrofluoric acid, deionized water and isopropyl alcohol mixed in a volume ratio of 1:3:1. The thickness of PS layers was roughly 1.8 μm . Volumetric porosity was determined by gravimetric measurements with the use of a Sartorius CP225D analytical semi-micro balance. As described in our previous works, the obtained PS layers contain a thin subsurface layer (about 0.3 μm from the topmost edge), which exhibits smaller pore sizes and lower porosity, significantly complicating pore filling [41,42]. Therefore, the layer in question was removed using a two-stage procedure which included chemical copper displacement deposition onto PS and subsequent dissolution of the deposited metal in nitric acid [43]. The latter process also causes oxidation of PS; as such, after subsurface layer removal, the PS samples

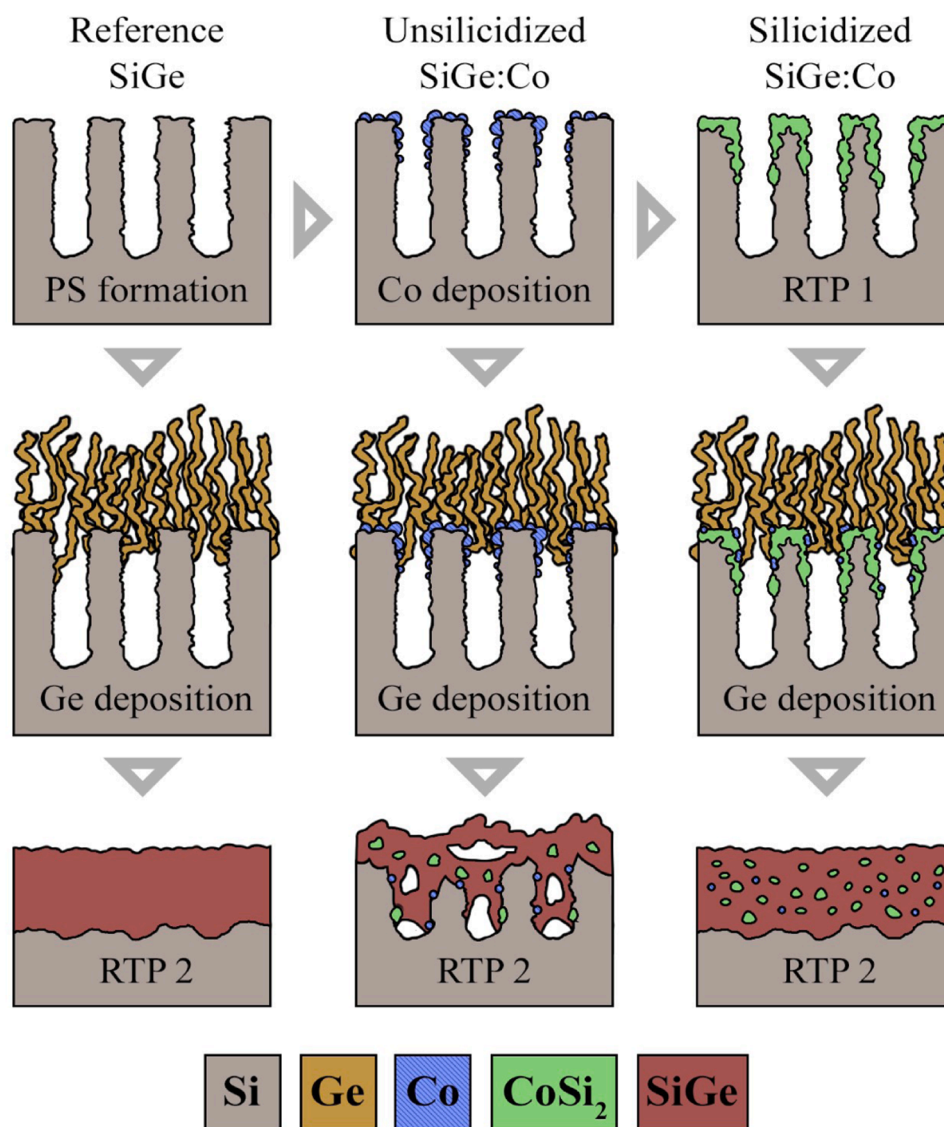


Fig. 1. Schematic illustration of processing stages involved in the fabrication of Si-Ge samples of various types, including two dedicated RTP stages for silicide formation (RTP 1) and alloy formation (RTP 2).

were immersed in concentrated hydrofluoric acid to dissolve the silicon oxide layer. All the samples discussed below have undergone this processing stage.

Cobalt was electrochemically deposited into the prepared PS layers using an aqueous solution containing 0.1 M $\text{CoSO}_4 \cdot 7\text{H}_2\text{O}$ and 0.4 M H_3BO_3 (pH = 2.86). The samples were kept in this electrolyte for one hour to ensure its access into the pores, followed by a single $65 \text{ mA}/\text{cm}^2$ current pulse. Subsequently to this stage, one sample group was subjected to an annealing procedure (RTP 1) with the use of an Annealsys As-One 100 RTP system to form cobalt silicide prior to germanium deposition. RTP 1 was conducted at 850°C over the course of 30 s under argon flow (800 sccm).

Germanium electrochemical deposition was carried out on preemptively air-dried samples using a solution containing 0.05 M GeO_2 , 0.5 M K_2SO_4 , 0.01 M InCl_3 and 0.1 M succinic acid. The deposition process was carried out for 60 min at a current density of $4 \text{ mA}/\text{cm}^2$ with constant stirring at 80°C , resulting in formation of germanium nanowires (GeNWs) in accordance with the electrochemical liquid-liquid-solid (e-LLS) growth mechanism.

RTP 2 was conducted under the same processing conditions as RTP 1 but in a different temperature/time regime. We have previously shown

[44] that GeNWs are prone to melting at lower temperatures compared to bulk germanium (938°C), which was also confirmed by additional experiments, the results of which are presented in supplementary materials (suppl. fig 1). These results indicate that partial melting of GeNWs arrays during RTP initiates at 650°C . At 850°C , most of germanium is vaporized with only some leftover spherical particles present on the surface. In turn, RTP conducted on a pristine PS sample (suppl. fig 2) indicates that the melting of PS is already observed at 950°C — much lower than the melting point of bulk silicon (1414°C). Thus, despite the lower melting points of the materials in question, most of the germanium is vaporized before PS even begins to melt. In order to increase the temperature stability of GeNWs and reduce germanium losses during annealing, an additional pre-treatment stage at 600°C should be introduced, as shown in our previous works [44–46].

Considering the above, RTP 2 was carried out in two stages: (1) pre-treatment at 600°C for 15 min and (2) primary treatment at 950°C for 30 s.

2.2. Analysis

The samples were studied by scanning electron microscopy (SEM)

using a Hitachi S-4800 scanning electron microscope equipped with a Bruker QUANTAX 200 spectrometer for energy dispersive X-ray spectroscopy (EDX) measurements. For distribution comparison, element concentration profiles were obtained by scanning each sample diagonally across the porous layer — the scan direction is indicated by a yellow arrow on the accompanying SEM images. The depth percentage values depicted on the profiles correlate to the start and end points of each arrow. It should be noted that this particular method of elemental analysis relies on acquiring the X-ray spectra from a volume of around $0.5 \mu\text{m}^3$. Since the structures in question generally fall below this size threshold, the data obtained via this method (EDX concentration profiles and maps) can be perceived as average throughout said volume and are therefore expressed in arbitrary units (a.u.). As the conditions of the EDX analysis remained unchanged for all the samples discussed in the present work, we consider this approach reasonable due to only using these concentration values as means of spatial distribution comparison.

A DRON-3M X-ray diffractometer was used for XRD analysis in CuK α radiation ($\lambda = 0.15406 \text{ nm}$) at room temperature, with an exposure time of 4 s and a step of 0.02° . XRD pattern matching was performed using PCPDF-WIN and Jana2006 software, as well as ICDD and COD databases.

Stokes Raman spectra were studied using an NTEGRA Spectra II confocal Raman spectrometer. Excitation was carried out by a He-Ne laser with constant pumping at a wavelength of $\sim 633 \text{ nm}$ and two semiconductor lasers emitting at wavelengths of 473 and 785 nm. The lasers were operated at 1.45, 1.00 and 8.60 mW of optical power, respectively. The spectra were recorded using a Peltier-cooled CCD detector. The radiation was focused on the sample using a $\times 100$ objective into a spot with a diameter of about $2 \mu\text{m}$. Temperature-dependent Stokes and anti-Stokes Raman spectra were recorded using a He-Ne laser with a Linkam THMS600 temperature control stage in the range of 100–500 K.

Study of electrical conductivity and Seebeck coefficient of SiGe alloy film samples was carried out in the temperature range of 80–450 K using a specialized Cryotel setup. To ensure stable contact of measuring probes to the samples and substrates, gold-antimony (AuSb) contact pads were pre-deposited onto the surface of SiGe. The pads were annealed in an argon atmosphere at 450°C for 20 min for improved electrical contact.

3. Results

3.1. SEM and EDX analyses

Fig. 2 shows surface and cross-section SEM images of the initial PS sample, as well as a corresponding EDX profile revealing silicon distribution along said cross-section.

Pore channel outlines can be clearly distinguished on the surface SEM image. By analyzing it with the use of ImageJ software, a pore density of $1.2 \cdot 10^{10} \text{ cm}^{-2}$, an average pore diameter of 95–100 nm, an average distance between pores of 90 nm, and an average sidewall

thickness of 5–7 nm were established. Gravimetric measurements indicate a volumetric porosity of 75 %. As can be seen from cross-section SEM images (Fig. 2, b), the pores possess cylindrical shapes and are perpendicular to the wafer's surface. The sidewalls exhibit a rough well-developed surface. Silicon's concentration in PS is about 30–35 a.u. in the subsurface region and gradually increases deeper into the layer as the signal from the monocrystalline wafer starts to accumulate.

Fig. 3 shows the results of the same set of measurements obtained for a PS sample after cobalt deposition.

As Fig. 3 would indicate, the surface of PS has undergone significant changes as a result of cobalt deposition. Pore entrances are still observed, but their average diameter has decreased to a value of 30–40 nm, with some pores completely obstructed by large cobalt particles. The metal is primarily concentrated on the surface and in the subsurface layers (roughly $1 \mu\text{m}$ from the surface), but can also be found in smaller quantities throughout the rest of the layer. These smaller metal particles are nearly indistinguishable on the SEM images. The EDX profile shows that the concentration of cobalt on the surface reaches 12 a.u. and decreases to 1 a.u. all the way at the pore bottoms. Cobalt's concentration being prevalent on the surface and rapidly decreasing with depth is most likely associated with significant diffusion limitations reducing the rate of reagent and byproduct transfer in and out of the pore channels, causing the solution inside the pores to be depleted in regards to cobalt ions and quickly stalling the deposition process.

SEM images of the same sample after RTP 1 for silicide formation are presented in Fig. 4 and exhibit some very minor changes in terms of surface morphology. A slight decrease in the number of exposed pores and an increase in the area covered with cobalt are observed.

For reference, SEM images of a PS sample without cobalt particles after germanium electrodeposition at different magnification levels are presented in Fig. 5. The resulting thick (up to $16 \mu\text{m}$) germanium layer consists of well-defined tangled GeNWs. Some germanium is present in the pores, but is predominantly located on the surface and in the subsurface areas. This is a direct result of germanium's growth primarily occurring on the simultaneously depositing indium particles in accordance with the ec-LLS mechanism as opposed to being subject to standard electrodeposition kinetics. In ec-LLS fusible metal particles act as both electron sources and growth mediums, promoting nucleation and growth of semiconductor crystallites inside or directly under them, usually resulting in a conglomeration of wires comparable with the fusible metal particles in question in terms of diameter [47].

SEM images of the samples at all stages of their processing are compiled in Fig. 6. The alloy films obtained in the cases of reference SiGe and silicidized SiGe:Co are homogeneous, with their thicknesses slightly varying across the cross-section from 0.8 to $1.5 \mu\text{m}$. They appear fused with the substrate and are discernible from it by their lighter color. The film/substrate interface is clearly distinguishable on the presented images and is mostly uneven, with characteristic bumps protruding up to 200 nm into the substrate. Similarly sized bumps are also observed on the films' surfaces. In contrast, the unsilicidized sample, despite being

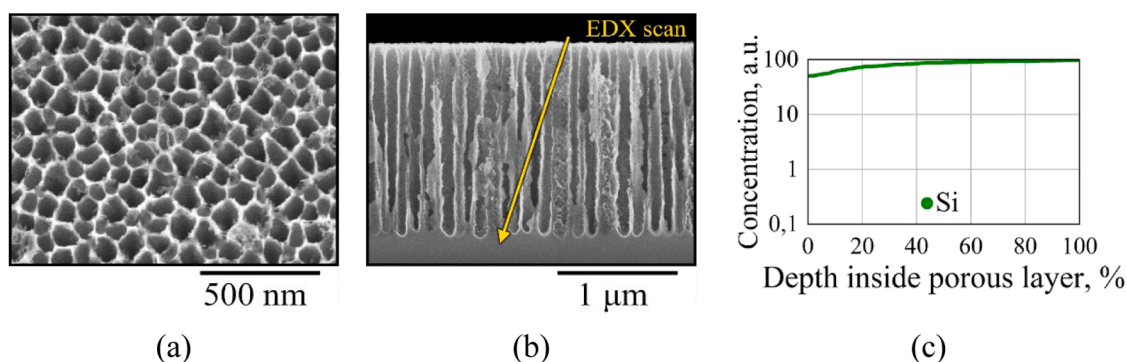


Fig. 2. Structure of the initial PS matrix: (a) plane-view SEM image, (b) cross section SEM image, (c) EDX-based silicon distribution profile along the layer's depth.

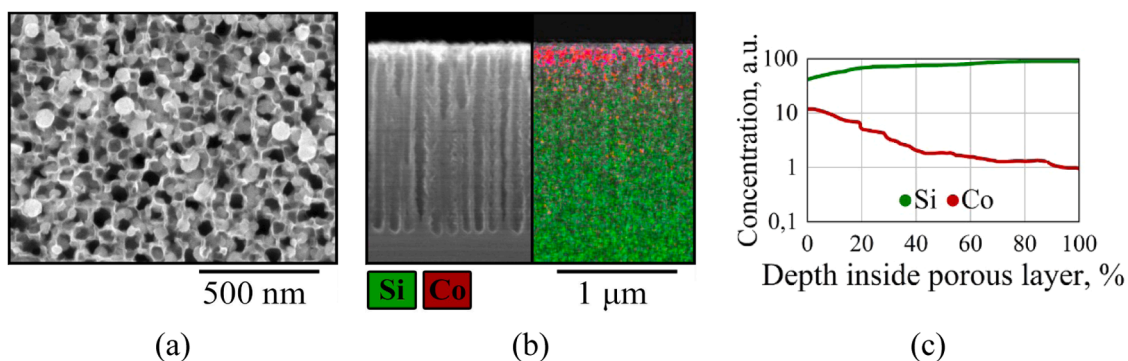


Fig. 3. Structure of the PS matrix with Co deposits: (a) plane-view SEM image, (b) cross section SEM image with corresponding EDX mapping results, (c) EDX-based silicon distribution profile along the layer’s depth.

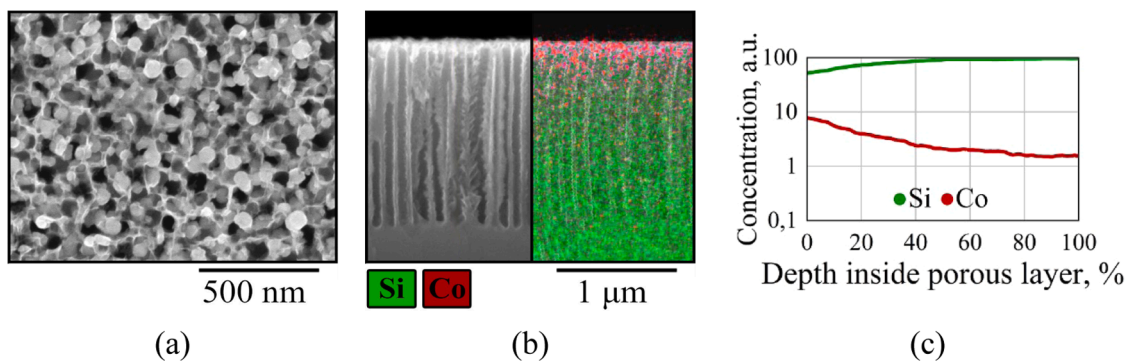


Fig. 4. Structure of the PS matrix with Co deposits after a preliminary RTP 1 stage for silicidization: (a) plane-view SEM image, (b) cross section SEM image with corresponding EDX mapping results, (c) EDX-based silicon distribution profile along the layer’s depth.

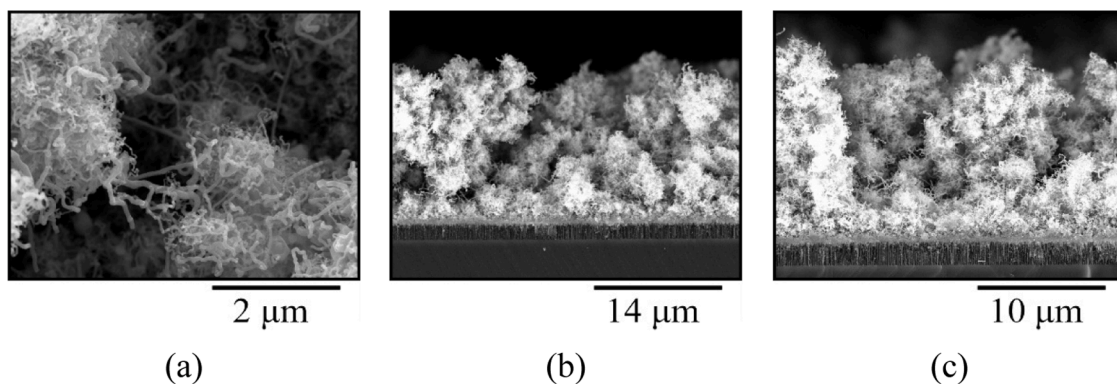


Fig. 5. Structure of the PS matrix after germanium electrodeposition: (a) plane-view SEM image, (b, c) cross section SEM images.

subjected to the same RTP 2 procedure, appears to retain most of the initial porous layer. It has a total thickness 2.2 μm, which comprises of a 1.8 μm PS remnant layer and a 0.4 Ge/SiGe layer on top of it. The layer possesses a non-dense structure with large cavities. The alloy film on top of the PS remnants exhibits a developed surface topography in the form of islands up to 0.5 μm in height and grooves of comparable size.

Fig. 7 shows surface SEM images of the same three samples. Evidently, the surface layer of reference SiGe appears to be the most even, with far less bumping compared to the other two samples. Silicidized SiGe:Co is comparable in thickness and also relatively uniform, though noticeably more granular. The surface of unsilicidized SiGe:Co is not continuous and riddled with many well-defined cavities, though some sections of the layer are interconnected.

According to EDX analysis results, concentration of germanium in reference SiGe slightly exceeds that of silicon over most of the sample’s

cross-section, amounting to 40 a.u. on the surface and remaining at that level until about 60 % into the layer, after which it starts to gradually decrease all the way down to 2.7 a.u. The silicon content gradually increases from 27 to 82 a.u. over the cross-section. In contrast, in silicidized SiGe:Co concentration of germanium is lower than that of silicon but more stable, and is primarily localized in the uppermost part of the film, amounting to 12 a.u. on the surface and slightly decreasing deeper into the layer. The concentration of silicon behaves similarly to the reference sample and gradually increases from 29 to 89 a.u. Cobalt is mostly localized on the surface, as indicated by a concentration of 6 a.u. that quickly falls off to a level of 1.5 a.u. at as little as 20 % depth and remains nearly unchanged afterwards.

In the case of unsilicidized SiGe:Co both germanium and cobalt are primarily localized in the subsurface area and start dropping after the 40 % point, with germanium decreasing from 35 to 3.5 a.u. and the metal

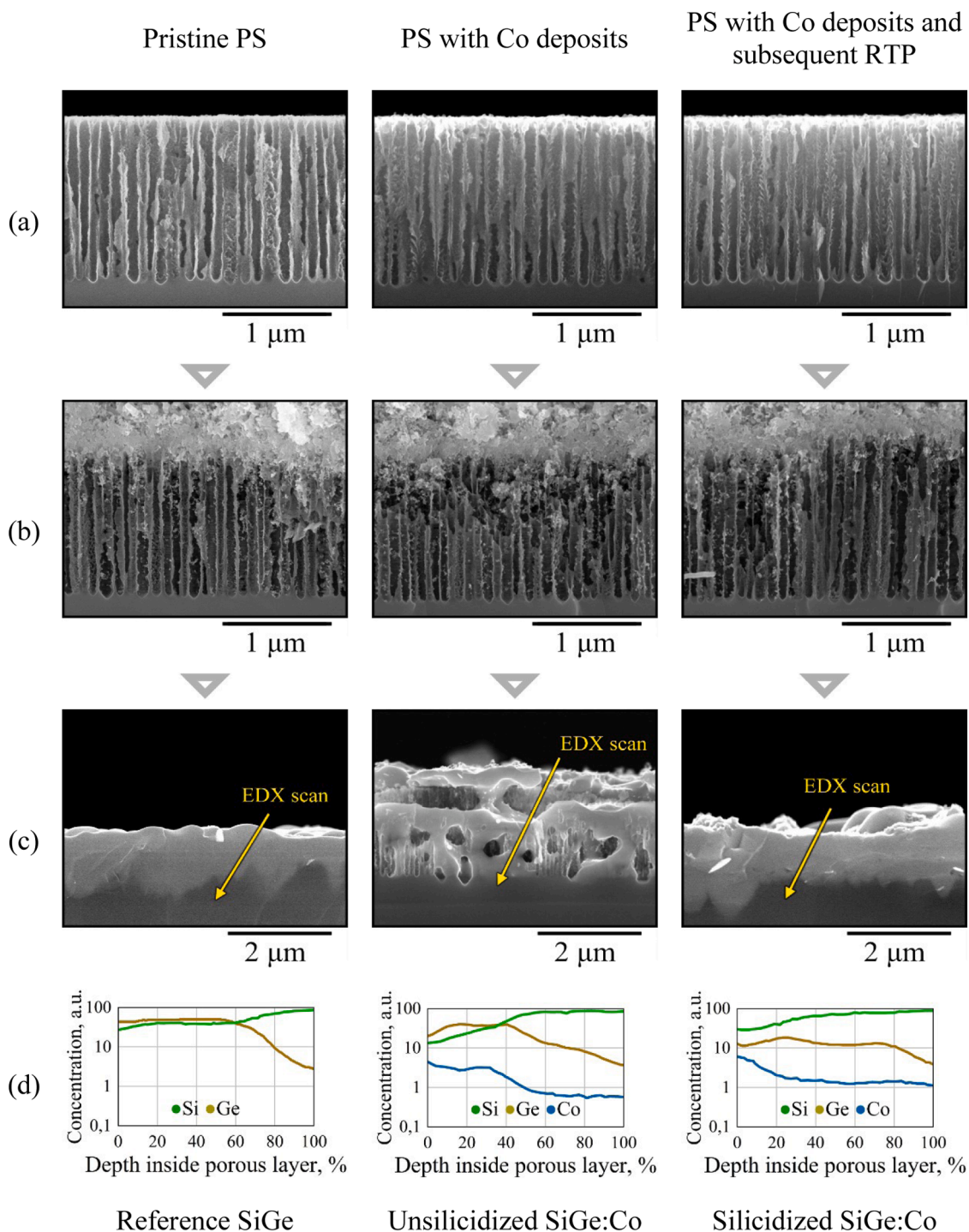


Fig. 6. SEM and EDX data acquired at different processing stages: (a) initial PS layers with or without Co before and after RTP 1, (b) PS layers after germanium electrodeposition, (c) alloyed layer after RTP 2, (d) EDX element distribution profiles inside said alloyed layers.

from 3 to 0.6 a.u. Both silicidized and unsilicidized SiGe:Co are characterized by smaller concentrations of germanium compared to the reference sample, most likely pertaining to the differences in GeNW growth mechanism when metal/silicide deposits are present on the surface.

3.2. XRD analysis

The samples' XRD spectra are compiled in Fig. 8. After depositing cobalt into PS and subjecting the layer to thermal processing at 850 °C, formation of CoSi₂ occurs — its presence is confirmed by prominent

peaks from the CoSi₂ (111) and CoSi₂ (220) planes. These are observed in both unsilicidized and silicidized samples, but are significantly more pronounced in the latter. Peaks from other cobalt silicides such as Co₂Si and CoSi were not detected, as the transition from CoSi to the high-temperature CoSi₂ phase begins at temperatures above 500 °C [48], which is significantly lower than the employed annealing temperature. Crystalline CoSi₂ possesses a fluorite cubic structure with a lattice constant of 0.5365 nm [49]. Peaks corresponding to CoSi₂ in the annealed PS/Co are located at 28.99° and 48.18°. The observed peaks are shifted towards higher diffraction angle values in relation to their relaxed positions of 28.81° and 47.92°, which implies disilicide lattice compression

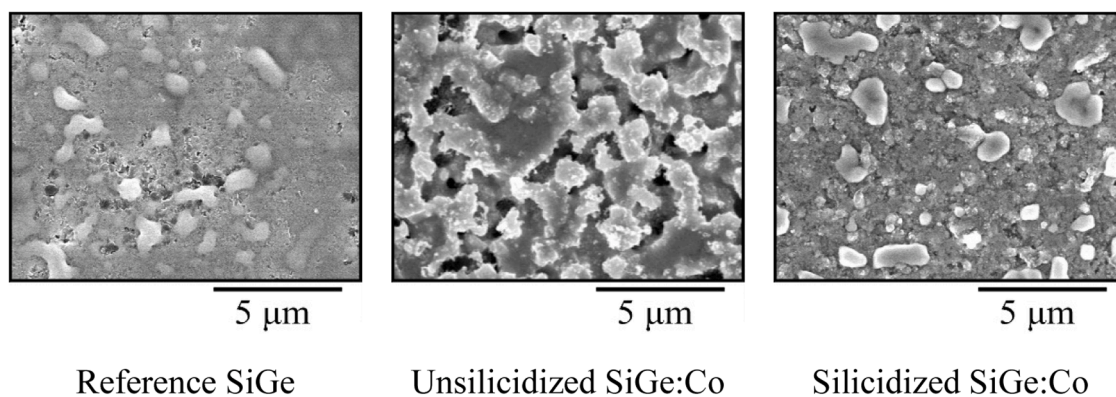


Fig. 7. Plane-view SEM images of the formed SiGe and SiGe:Co films.

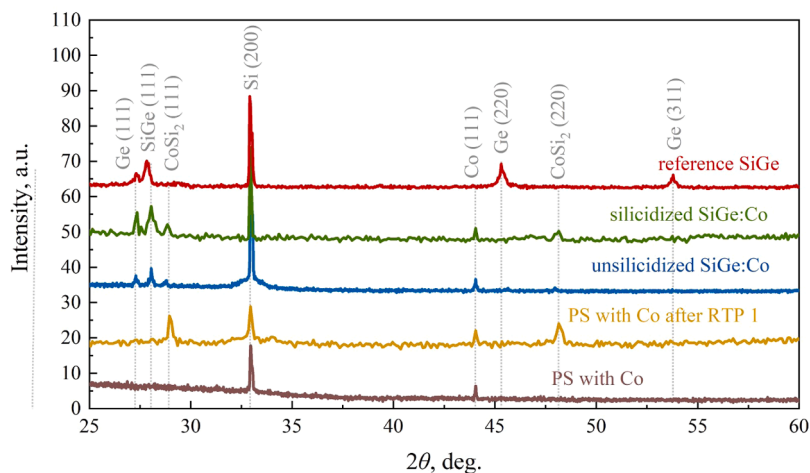


Fig. 8. XRD patterns of various samples. The peaks are identified using the ICDD (Co — #00-015-080, Si — #00-027-1402, Ge - #00-004-0545, CoSi₂ — #00-038-1449) and COD database (SiGe — #96-153-7803).

strain of about 0.5 % in these directions. The lattice strain of CoSi₂ in unsilicidized and silicidized samples determined using the same approach does not exceed 0.1 %.

The reflection peak at $2\theta = 44.05^\circ$ suggests that metallic cobalt particles are present in the samples even after RTP 2. According to the corresponding Pourbaix diagram [50], cobalt is expected to only be present in its metallic form after electrolysis of a Co²⁺-containing aqueous solution with a pH value of 2.86, which is further evidenced by SEM and XRD results confirming the presence of metallic crystals. Evidently, not all the deposited cobalt reacted with silicon to produce silicide compounds in either sample. Contrary to CoSi₂ peaks, the intensity of this one remains unchanged in the silicidized sample.

Some peaks are present beyond the presented 2θ range, but are not included in Fig. 8 due to being largely irrelevant to the discussion. A high intensity peak at $2\theta = 69.35^\circ$ and a smaller peak at $2\theta = 32.85^\circ$ correspond to (400) and (200) planes of the silicon substrate. The positions of these peaks subsequently to cobalt deposition and annealing at 850 °C for 30 s are shifted towards smaller angles, implying that the porous layer is preserved after this procedure due to its lattice being broadened compared to the bulk monocrystalline silicon [51]. The lightly-pronounced peak seen in some samples at 61.73° is a satellite to the one observed at 69.35° and is associated with diffraction from Si (400). A broad band with a maximum at around $2\theta = 22.25^\circ$ present in some of the samples is associated with amorphous SiO₂ and is most strongly defined in the reference SiGe sample. However, little to no differences in oxygen contents were detected during EDX measurements, so we do not expect this factor to affect its properties in any

substantial way.

After germanium deposition and RTP 2, additional peaks at $2\theta = 27.31^\circ$ and 28.06° emerge. They correspond to reflections from germanium (111) and SiGe (111) planes, as indicated on the figure. Presence of small amounts of unalloyed crystalline germanium is possible in the employed temperature regime and was previously observed during the formation of SiGe using the method in question [52]. The lattice constant of the obtained SiGe is calculated to be $a_{\text{SiGe}} = 0.5503$ nm. Considering $a_{\text{Si}} = 0.5431$ nm and $a_{\text{Ge}} = 0.5658$ nm [53], according to Vegard's law ($a_{\text{SiGe}}(x) = (1-x)a_{\text{Si}} + xa_{\text{Ge}}$) this corresponds to $x = 0.3172$ germanium fractions in the alloy [54,55]. Additionally, in the reference sample, germanium is also present in (220) and (311) crystalline orientations (45.31° and 53.79° , respectively), indicating differences in growth mechanism caused by the presence of metal or silicide particles on the surface.

Taking the above into account, the obtained SiGe:Co films could be considered polycrystalline and consisting of SiGe and cobalt disilicide crystallites with residual cobalt and germanium inclusions. However, the FWHM of all peaks observed on the XRD plots is relatively small, and the crystalline size calculated using the Sherrer equation exceeds 200 nm, making it impossible to determine particle sizes using this method.

3.3. Raman spectroscopy measurements

Stokes Raman spectra recorded at different excitation wavelengths revealed a number of bands corresponding to characteristic vibrational modes of the bonds in silicon-germanium alloys (Fig. 9). Since longer

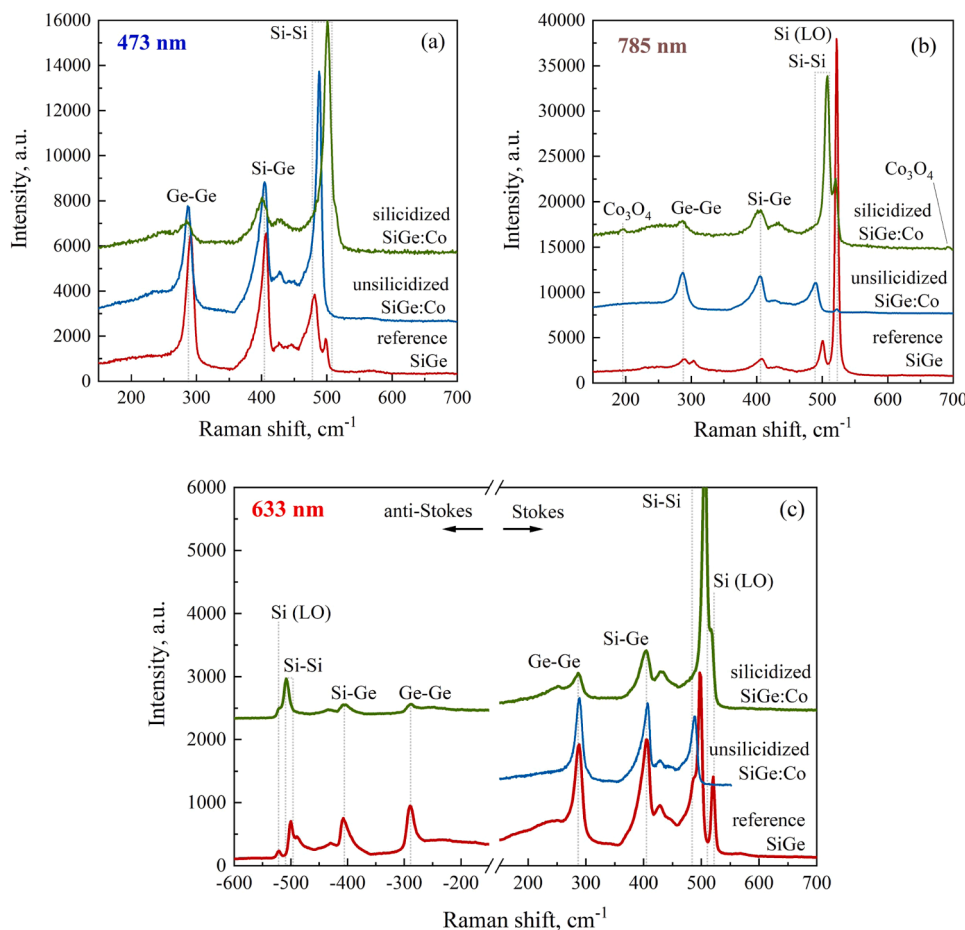


Fig. 9. Stokes Raman spectra of the alloyed samples measured with (a) 473 and (b) 785 nm lasers and (c) Stokes and anti-Stokes Raman spectra of the same samples measured with a 632 nm laser.

wavelength radiation can penetrate further into a sample's volume, using lasers with different wavelengths allowed us to collect data from varying depths of the obtained films. According to data presented by J. Humlíček et al. [56], the absorption depths for 473, 633 and 785 nm laser radiation into an alloy with a germanium content of 40 % are determined to be about 80 nm (i.e. only the surface of the film will be analyzed), 4 μm (the entire layer) and $>5 \mu\text{m}$ (the substrate/alloy interface), respectively.

The band with the most unstable position corresponds to Si-Si bonds in SiGe [57]. Its position shifts from 500 cm^{-1} for reference SiGe sample to 489 cm^{-1} for unsilicidized SiGe:Co and up to 508 cm^{-1} for silicidized SiGe:Co. The second Raman band at around $286\text{--}290 \text{ cm}^{-1}$ corresponds to Ge-Ge bonds in a SiGe alloy [44]. Notably, in the case of the reference SiGe at 785 nm, a secondary band is observed at 303 cm^{-1} , which, in accordance with differences in laser penetration depth, indicates presence of some unalloyed germanium in the bottommost parts of the alloy layer. Lastly, the third band located at $404\text{--}406 \text{ cm}^{-1}$ is associated with Si-Ge bonds [58]. All the aforementioned bands are asymmetrical, which indicates involvement of low-dimensional effects, surface states, defects, or non-stoichiometric composition of the material [59,60]. Alloy formation is accompanied by a change in the length and energy of vibrations of bonds between silicon and germanium atoms, and a shift in the corresponding band positions from their base values is observed (521 cm^{-1} for monocrystalline silicon and 300 cm^{-1} for crystalline germanium) [61].

Weakly-defined bands present in the Raman spectrum of the silicidized SiGe:Co sample at 196 and 690 cm^{-1} upon excitation by a 785 nm laser are related to Co_3O_4 [62]. Given the samples' exposure to air subsequently to cobalt deposition, oxide formation is inevitable, and a 1

nm film of $\text{Co}(\text{OH})_2$ is known to form instantly at room temperature [63]. In turn, $\text{Co}(\text{OH})_2$ is converted into Co_3O_4 at temperatures above $310 \text{ }^\circ\text{C}$ [62], and the short annealing stage at $950 \text{ }^\circ\text{C}$ likely wasn't sufficient to convert it to CoO . No peaks corresponding to the Raman-inactive CoSi_2 phase or other silicides were observed.

Additionally, reference SiGe and silicidized SiGe:Co samples also exhibit an intensive band located at around 521 cm^{-1} , which corresponds to the triple-degenerate optical vibrational mode of monocrystalline silicon Si (LO) at the center of the Brillouin zone [61]. Since this band is not observed under 473 nm laser radiation, it can be assumed to originate from the silicon substrate, which the lower-wavelength radiation does not reach. Additionally, a Si (LO) band is not observed for unsilicidized SiGe:Co due to its high absorption.

It is known that in $\text{Si}_{1-x}\text{Ge}_x$ alloys with random distribution of silicon and germanium atoms the probability of Ge-Ge, Si-Ge, and Si-Si bond formation is proportional to x^2 , $2x(1-x)$ and $(1-x)^2$, respectively [62–65]. Therefore, the integral intensities of each of the three scattering bands observed on the Raman spectra (which correspond to respective atomic bonds in the SiGe alloy) should linearly depend on the number of respective bonds. Deviations from linearity depend on the magnitude of phonon-induced atomic displacements, the derivative of bond polarizability with respect to this displacement, and the Bose factor. Hence, the ratio of band intensities in the Raman spectra can be expressed as follows:

$$\frac{I_{\text{Ge-Ge}}}{I_{\text{Si-Ge}}} = \frac{Bx}{2(1-x)} \quad (1)$$

$$\frac{I_{Si-Si}}{I_{Si-Ge}} = \frac{A(1-x)}{2x} \quad (2)$$

Coefficients A and B are introduced to compensate for resonance effects that lead to the dependence of band intensity on excitation wavelength. They widely vary from 1 to 4 for different ranges of Ge contents in the alloy and excitation wavelengths [64–67]. Here we adopted the values of $A = 1.5$ and $B = 1.8$ from [67], which correspond to the widest possible range of SiGe alloy compositions. Germanium contents calculated using Raman spectra obtained at different excitation wavelengths are presented in Table 1.

The use of lasers with different wavelengths made it possible to reveal the change in germanium concentration along the depth of the obtained SiGe films. In the reference SiGe film the germanium fraction x does not change with depth and ranges from 0.510 to 0.529. In unsilicidized SiGe:Co germanium concentration increases along the layer depth from 0.464 to 0.572. Lastly, silicidized SiGe:Co demonstrates opposite behavior, with concentration decreasing from 0.301 to 0.210 along with depth and remaining below values found in all other samples. The obtained germanium fraction in the silicidized sample is close to the value calculated using the position of the SiGe (111) XRD peak. Its composition is estimated to be the closest to $Si_{0.8}Ge_{0.2}$, which is considered to be optimal for thermoelectric applications [13].

Stokes and anti-Stokes Raman spectra represent processes involving emission and absorption of phonons. The intensity ratio of corresponding non-resonant peaks is proportional to phonon population. The sample's temperature can be calculated using Boltzmann statistics [68], and the alloy film temperature can be determined from localized vibrational modes. The difference between the film temperature and the temperature of the silicon wafer underneath it ΔT can be determined using the alloy's thermal conductivity κ , the supplied power P , and the thickness of the absorbing region of the film L in the direction perpendicular to the surface with a cross-sectional area A . Therefore, according to Fourier's law, thermal conductivity is equal to

$$\kappa = \frac{P}{\Delta T} \frac{L}{A} \quad (3)$$

As can be derived from Fig. 6, the film-substrate interface exhibits a highly developed topography, causing the film's thickness to vary greatly. Therefore, to obtain an average result, the laser beam area was expanded to a diameter of about 7 μm and the power was increased to 2.4 mW during thermometric Raman measurements. These values were then used to calculate κ using Eq. (3). The average alloy film thickness, determined from Fig. 6, was employed as L , and the temperatures determined from Si-Si Raman peaks from the substrate and film were used to calculate ΔT .

Strong absorption in the unsilicidized sample is attributed to its cavernous structure, which causes significant light scattering within the layer due to multiple reflections in said cavities (Fig. 6). This did not allow us to reliably register the anti-Stokes part of the Raman spectrum and determine the substrate's temperature. Therefore, we were unable to evaluate the thermal conductivity and ZT values of the unsilicidized sample.

Table 1

Germanium fractions in various SiGe alloy samples calculated based on Raman spectroscopy data.

Sample	Laser wavelength, nm	Germanium fractions x in $Si_{1-x}Ge_x$
Reference SiGe	473	0.519
	633	0.510
	785	0.518
Unsilicidized SiGe:Co	473	0.464
	633	0.542
	785	0.572
Silicidized SiGe:Co	473	0.301
	633	0.300
	785	0.210

The dependency of the resulting alloy films' thermoelectric parameters on temperature is illustrated by the plots presented in Fig. 10. The obtained thermal conductivity values (Fig. 10, d) are significantly lower than the room temperature values for bulk silicon and germanium ($156 \text{ WK}^{-1}\text{m}^{-1}$ and $\sim 60 \text{ WK}^{-1}\text{m}^{-1}$, respectively) [69]. The measured values of the alloy films' thermal conductivity are lower than those of bulk SiGe alloys of similar compositions and are comparable to values recorded for thin-film samples in other works [13].

Measurements of the samples' resistivity in a temperature range of 80 to 470 K revealed it to be higher compared to the initial n+-Si substrate (Fig. 10, a). As such, it is not possible to employ a simple bilayer conductivity model of two conductors connected in parallel (film/substrate) in order to determine a given film's contribution to the conductivity and Seebeck coefficient. An increase in resistivity in a case when a conductive film is formed on a conductive substrate may be caused by the current exclusively passing through the film due to a potential barrier present at the film/substrate interface.

These results are in agreement with our previous studies [70], where it was shown that the utilized method of SiGe alloy formation enables fabrication of n- or p-type SiGe by using a silicon substrate with the corresponding type of dopant as a base. Assumingly, in this case the absence of current flow into the substrate is caused by the formation of a heterobarrier at the SiGe alloy/silicon substrate interface. The height of such a barrier varies depending on the state of silicon (strained or relaxed), as well as on the germanium content in the alloy, and, in the case of a relaxed substrate and SiGe with 30 % germanium, is estimated to be 30 meV for electrons and 230 meV for holes [71]. In [72] it was shown that a SiGe rectifier comprised of a SiGe layer on n-type Si demonstrates approximately two orders of magnitude less leakage current compared to a Schottky rectifier. In the case of the Si/CoSi₂ interface, a Schottky barrier of about 630 meV is also formed [73]. As such, regardless of the Si/SiGe or Si/CoSi₂ interface structure, there will always be a barrier forcing the current to exclusively flow through the film.

Given this lack of the substrate's shunting influence, thermal electromotive force (EMF) measurement results are expected to reflect the processes occurring in the film. This assumption is supported by unsilicidized SiGe:Co possessing the highest resistivity, as well its temperature dependence sharply changing its incline at about 200 K. The cavernous structure of this sample's film significantly increases the scattering of charge carriers. When unsilicidized SiGe:Co is shunted by the substrate, the current would flow through the latter, causing the sample's resistivity to not deviate far from the substrate's.

We can speculate that the results of resistivity and thermal EMF measurements reflect processes occurring in the film. However, since we are unable to strictly separate film and substrate inputs at this stage of research, we will consider the samples' electrical conductivity and Seebeck coefficient values as effective parameters with contributions from both. In the worst-case scenario, such an approximation may overestimate the film's electrical conductivity and underestimate its thermal EMF. The resistivity values of reference SiGe and silicidized SiGe:Co samples are almost the same across the studied temperature range and are approximately 10 % higher than those of the substrate. The difference in Seebeck coefficient S , on the other hand, is much more pronounced, with S reaching $-450 \mu\text{V/K}$ in silicidized SiGe:Co at 450 K — a twofold increase over the substrate's value of $-271 \mu\text{V/K}$ (Fig. 10, b).

Unsilicidized SiGe:Co exhibits the lowest Seebeck coefficient among all samples. This behavior is of some interest, because if the increase in this sample's resistivity is associated with an effective decrease in majority charge carrier concentration, then the Seebeck coefficient should increase in accordance with the Pisarenko relation

$$S = \frac{8\pi^2 k_B^2}{3eh^2} m^* T \left(\frac{\pi}{3n} \right)^{2/3}, \quad (4)$$

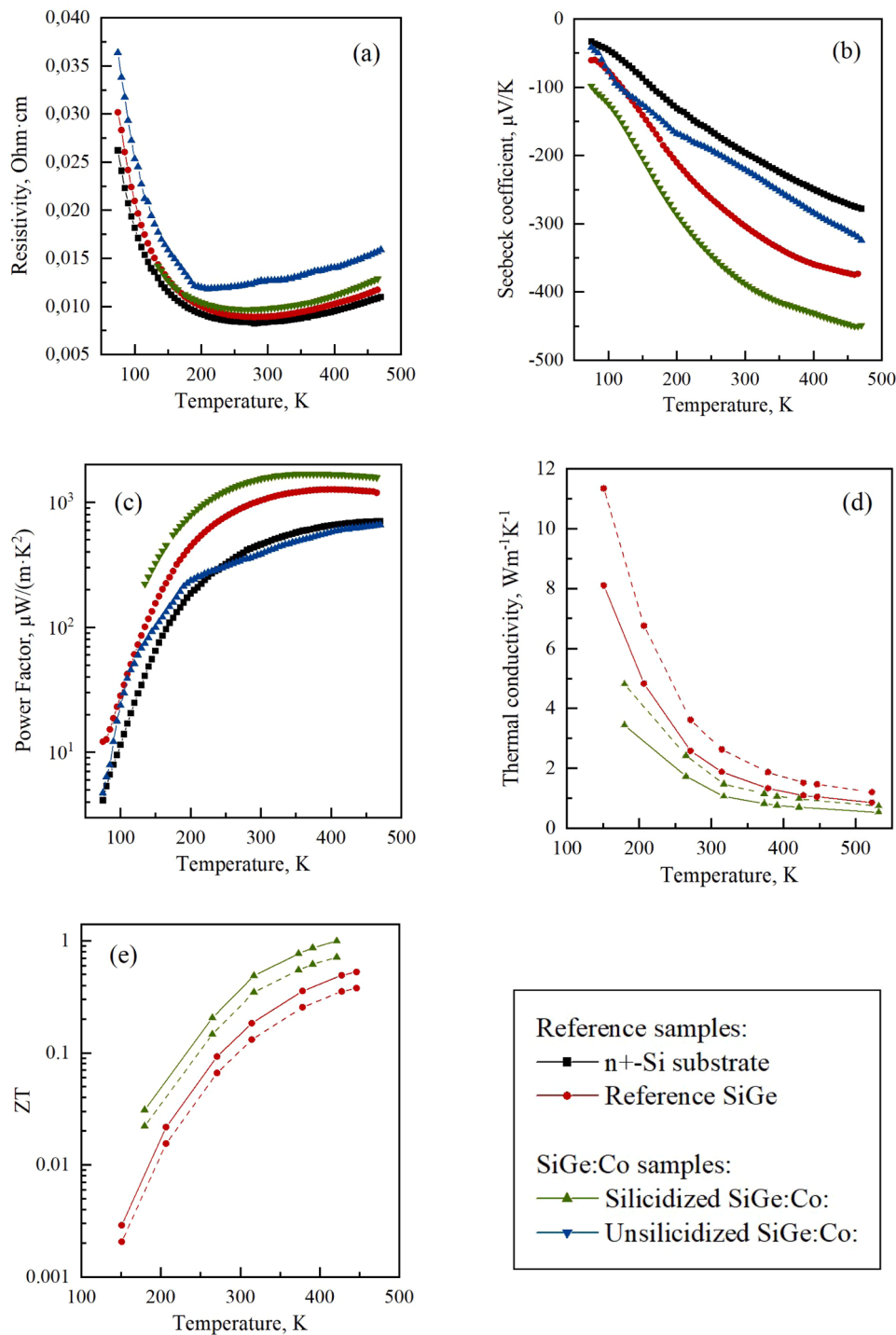


Fig. 10. Temperature dependency of (a) resistivity, (b) Seebeck coefficient, (c) power factor, (d) thermal conductivity and (e) ZT for pristine silicon and SiGe samples obtained thereon. Dashed lines indicate values corrected to account for non-Fourier phonon heat conduction, as described in Section 4.2.

where k_B is the Boltzmann constant, h — the Planck constant, n — the carrier concentration, e — the carrier charge, m^* — the effective mass of the carrier.

Moreover, as shown in [13] for a large-area $\text{Si}_{0.8}\text{Ge}_{0.2}$ nano-meshed film, thermal EMF increases along with pore diameter up to 300 nm. As can be derived from Fig. 6, unsilicidized SiGe:Co possesses pores of approximately the same size. The simultaneous drop in electrical conductivity and thermal EMF may be due to the emergence of charge carriers of an opposite sign; however, no such carriers were introduced into the sample, even unintentionally, since the other samples show a

significant increase in thermal EMF even at a much smaller increase in resistivity. It's plausible that, unlike the ideal structure described in [13], high surface state density on the pore sidewalls of the unsilicidized sample creates local conductive channels, shunting the thermal EMF. As a result, the sample's power factor at temperatures above 250 K becomes even lower than that of the silicon substrate (Fig. 10, c). In contrast, the power factor of silicidized SiGe:Co is the highest among all the samples and reaches values of 1600–1700 $\mu\text{W}/(\text{m}\cdot\text{K}^2)$ at room temperature.

4. Discussion

4.1. Silicide and alloy formation

To summarize, the samples discussed in this study were formed by subsequently depositing cobalt nanoparticles and GeNWs into PS matrices from aqueous solutions containing cobalt and germanium ions, respectively, and optionally subjected to RTP 1 to additionally promote cobalt silicide formation. As a result, three types of composite structures were obtained: reference PS/GeNWs, PS/Co/GeNWs and PS/CoSi₂/Co/GeNWs, which were subsequently subjected to RTP 2 to obtain SiGe alloys. It should be noted that, since GeNWs are predominantly located on the surface of PS rather than inside the pores, alloying will inevitably initiate on the surface and occur from top to bottom.

Assumingly, a continuous alloy layer was not formed in the unsilicidized sample due to insufficient amounts of germanium compared to the other two cases, as indicated by mass measurements. Specifically, the mass of germanium deposited onto the unsilicidized sample was almost three times less than that for other samples, despite utilizing the same processing regimes. In addition, the alloying process is heterogeneous, and in some areas of the film also reached the lower layers, which led to the formation of cavities in the alloy. Such a drastic difference in the mass of deposited germanium might be related to the change in the surface of PS after cobalt deposition, which in the case of silicidized SiGe:Co is somewhat alleviated after RTP 1. The presence of cobalt could drastically alter the electrochemically-active surface of the sample in question, greatly affecting local current density and thus the resulting morphology. A more detailed explanation of this phenomenon requires additional studies which are beyond the scope of this particular work.

Preliminary annealing at 850 °C for 30 s provided strictly solid-phase formation of cobalt silicides, as the melting point of any silicides in the Co-Si binary system exceeds 1200 °C [74]. This contributed to the re-opening of some of the pores on the surface of PS, additionally encouraging germanium filling. The distribution of cobalt appears to be nearly unaffected by RTP 1, which can be attributed to the use of a relatively low temperature and processing time. This case is additionally supported by Raman spectroscopy data: germanium content in the alloy registered at different laser wavelengths remains largely unchanged, while germanium concentration deep in the volume of silicidized SiGe:Co is significantly lower than that on its surface (Table 1).

As shown by d'Heurle et al. [48], formation of CoSi₂ requires a sufficiently high activation energy of 2.6 eV and involves several mechanisms occurring simultaneously: nucleation, diffusion and (presumably) interface reaction. Activation energy is increased even further in the presence of Ge, as the CoSi₂ phase forms at progressively higher temperatures as Ge content is increased [35]. Since silicide formation occurs in a strict sequence from Co₂Si to CoSi₂ [48], the increase in nucleation temperature could be attributed to the difference in the entropy of mixing caused by the consumption of Si originating from SiGe and formed by the expulsion of Ge previously dissolved in CoSi [35].

Thus, despite the high annealing temperature of unsilicidized and silicidized samples, the short duration of RTP 2 did not enable the formation of sufficient amounts of CoSi₂ in unsilicidized SiGe:Co, which is expressed in the weak intensity of corresponding XRD peaks and high intensity of the peak corresponding to pristine Co. As such, a preliminary silicidization stage can be deemed crucial in order to obtain a continuous SiGe alloy film containing CoSi₂.

The presence of cobalt precipitates in the annealed PS with Co sample can be explained by an excessive amount of cobalt for the synthesis parameters used. In [35] the duration of annealing, after which cobalt was completely changed into cobalt silicide was also 30 s, but the maximum thickness of metal films was only 10 nm. In our case, the pore sizes ranged from 40 to 100 nm [52], and a 30 s annealing process was not enough to fully convert all of the metal into silicide.

4.2. Thermoelectric parameters

Characterization of thermoelectric materials is a challenging task involving measurement of both their electrical and thermal properties. It is further complicated in the case of film materials. Traditionally, thermal conductivity of thin films is measured using time-domain (TD), and frequency-domain (FD) methods. TD exhibits high quantitative reliability and allows to perform in-plane and cross-plane thermal conductivity measurements, but is sophisticated and requires complex signal analysis and expensive optics [75]. FD assumes heat dissipation from a Joule-heated metal strip, which must be formed on the sample's surface by photolithography, which greatly complicates its preparation and is not always possible to apply to rough surfaces. Measurement of transverse thermal conductivity by this method is relatively easy, but in-plane thermal conductivity determination requires fabrication of bridge structures, which is a non-trivial task that requires correct accounting for heat dissipation. Processing of experimental results obtained with the FD method is also difficult and requires the use of multi-parameter models [76].

The Raman thermometry method employed in this work enables acquisition of a given film's thermal conductivity using Boltzmann statistics and Fourier's law of thermal conductivity. Previously, the suitability of this method was demonstrated for samples of similar composition and structure (SiGe films on silicon substrates) — both in other works [77] and in our own previous publications focused on determining thermal conductivity of SiGe formed using the proposed method at room temperature [78]. The errors in thermal conductivity determination using this approach are usually related to the measurement of film and substrate temperatures, as well as to the deviation of heat transfer processes from Fourier's law. In the first case, it is important to provide non-resonant conditions for Raman spectrum acquisition, as well as correctly determine the intensity of the corresponding Stokes and anti-Stokes peaks.

In our experiments, we used a laser with a wavelength lying far from the resonant inelastic scattering bands of the studied vibrational modes [79], and fitting of closely located bands in the 500–520 cm⁻¹ region by the Voigt profile was employed. The validity of such a procedure was confirmed by experiments previously performed on pure monocrystalline silicon and germanium substrates. The main error of thermal conductivity determination can be attributed to non-Fourier phonon heat conduction. In [80] it is shown that, if bulk silicon is locally heated (starting from the characteristic heat source size of about 100 μm), the measured thermal conductivity value decreases due to ballistic phonon transport. Since monocrystalline silicon and SiGe possess the same lattice type, we can use the data from [80] to evaluate the contribution of this effect to our results in regards to silicon. In our case, the laser beam spot size was about 7 μm, so the calculated thermal conductivity for our samples (Fig. 10, d, solid lines) can be underestimated by 40 %. As such, in the following discussion, thermal conductivity values will be corrected to account for this factor (Fig. 10, d, dashed lines) and used to calculate ZT.

4.3. Thermal conductivity measurements

Thermal conductivity values obtained for reference SiGe and SiGe:Co samples are significantly smaller than the room temperature thermal conductivities for bulk silicon and germanium (156 WK⁻¹m⁻¹ and ~60 WK⁻¹m⁻¹, respectively) [69]. Evidently, thermal conductivity decreases along with an increase temperature due to enhanced phonon-phonon scattering. The nature of this dependence coincides with the literature data for monocrystalline SiGe fabricated using the Czochralski method [81] and pressure sintering [82]. In absolute values, thermal conductivity of reference SiGe at 300 K is 3 Wm⁻¹K⁻¹, which is 2–4 times less than that of bulk SiGe alloys of similar composition [79, 80], and is at the same level as some experimental values obtained for thin-film samples (see [13] and references therein). These results are in

good agreement with the calculations of thermal conductivity of SiGe thin films found in [83] for SiGe of various compositions, where it was shown that thermal conductivity decreases with film thickness mainly due to boundary scattering being the dominant process.

Thermal conductivity of both SiGe:Co samples is smaller than that of reference SiGe over the whole investigated temperature range (Fig. 10, d). This can be attributed to additional phonon scattering at the boundaries of cobalt disilicide nanocrystals. Nanostructuring itself provides scattering of phonons with short and medium wavelengths (up to 100 nm), while long-wavelength phonons propagate in the material unimpeded. Taking into account that in SiGe the primary contribution to thermal conductivity is made by long-wavelength phonons [83], formation of a nanocomposite material with grain sizes larger than 100 nm should significantly reduce its thermal conductivity. Narrow peaks corresponding to Ge, Co and CoSi₂ on XRD spectra in SiGe:Co samples indicate the presence of precipitates of similar sizes.

No results in regards to the effect of submicron-sized cobalt disilicide precipitates on the thermal conductivity of SiGe alloys are published in literature. However, in [31] a 20–25 % reduction in silicon thermal conductivity was shown upon introduction of 50 to 500 nm CoSi₂ precipitates, and similar thermal conductivity behavior between the silicidized sample and the sample with CoSi₂ precipitates was also demonstrated. Additional evidence of the determining role of precipitates in the reduction of thermal conductivity for silicidized SiGe:Co lies in the large difference in thermal conductivity at low temperature, when disilicide nanocrystals provide effective phonon scattering.

CoSi₂ possesses a fluorite structure with a lattice constant of 0.5356 nm, which is 1.3 % smaller than that of silicon. Since a SiGe alloy of any composition has a lattice constant greater than that of silicon, the difference between it and the lattice constant of cobalt disilicide will be even greater, and CoSi₂ precipitates inside SiGe are expected to exhibit tensile strain. However, according to the XRD data, the CoSi₂ lattice was almost relaxed in both silicidized and unsilicidized SiGe:Co samples. Based on this we can conclude that a high density of dislocations appears at the interface in the form of a local nanoscale disorder, which should provide efficient scattering of short-wavelength phonons. As such, the observed decrease in thermal conductivity in silicidized SiGe:Co can be attributed to phonon scattering at various length scales.

4.4. Resistivity measurements

In accordance with our measurements, the resistivity of the initial silicon wafer, upon which the alloys in question were formed, amounted to 0.008 Ohm-cm, which is well within the doping level tolerance in regards to the manufacturer-specified value of 0.01 Ohm-cm and is. The resistivity values of reference SiGe and SiGe:Co samples at temperatures below 170 K do not deviate from this number, but raising the temperature past this point leads to an increase in resistivity of SiGe:Co by about 10 %. Since cobalt precipitates are observed in both unsilicidized and silicidized SiGe:Co, it can be assumed that the metal may also be present in these samples in the form of individual atoms. In this case, the increase in resistivity of the silicidized sample may be attributed to ionization of these cobalt atoms, which provides deep-level n- and p-type traps near the middle of the band gap in both silicon and germanium [84], which leads to the depletion of majority charge carriers in the sample. It is known that cobalt disilicide CoSi₂ exhibits one of the largest electrical conductivity values among transition metal silicides [85]; however, formation of space charge and mismatch dislocations on the SiGe/CoSi₂ heterojunction can also lead to charge carrier scattering in a wide temperature range.

Among the investigated samples, unsilicidized SiGe:Co exhibits the largest resistivity and possesses a thermal EMF value similar to that of bulk silicon. As a result, its power factor outperforms that of the substrate only at temperatures below 200 K, when its resistance is not significantly different from the substrate in both magnitude and variation (Fig. 10, a). It is quite possible that the thermal conductivity of such

a sample may be even lower than that of silicidized SiGe:Co due to its cavernous structure; however, as already mentioned, the high absorption of the laser signal did not allow us to reliably register the anti-Stokes part of the Raman spectrum and determine the substrate's temperature. Therefore, this sample was not used for further analysis.

4.5. Seebeck coefficient measurements

The thermal EMF value of a pure SiGe alloy strongly depends on the material's doping level, ratio of germanium and silicon, and the way the sample is fabricated [18,80,84]. The value registered in our experiments for reference SiGe, as well as its temperature dependence coincides well with the literature data for alloys of similar composition and conductivity.

In accordance with the expression (4), which is fully confirmed experimentally, in doped SiGe alloys thermal EMF increases along with a decrease in charge carrier concentration. In our case, the resistivity of silicidized SiGe:Co increased in relation to the reference sample (Fig. 10, a). If we were to estimate the corresponding decrease in concentration using the results from [55], it would not be enough to provide the observed increase in thermal EMF (Fig. 10, b). On the other hand, if we assume that the increase in resistivity is caused by the compensation of majority charge carriers in the alloy by a dopant with an opposite sign, then thermal EMF should be expected to have decreased due to bipolar electrical conductivity. In doped semiconductors, thermal EMF can also increase in the presence of sharp local densities of states of electrons around the Fermi levels near energy band edges [86]. However, the sample's resistivity should not increase in such a case.

The most likely reason for the strong increase in thermal EMF for silicidized SiGe:Co is the energy filtering effect, which involves strong scattering of low-energy charge carriers on potential barriers due to a steep dependence of their relaxation time on energy [20,55,86]. No information on the SiGe/CoSi₂ Schottky barrier was found in literature, but, as mentioned above, is about 630 meV in the case of Si/CoSi₂ [72, 83]. Considering that the work function of SiGe lies in the range between those of pristine Si and Ge, which differ by about 500 meV (or no more than 200 meV for a composition similar to silicidized SiGe:Co) [87], then it can be argued that the SiGe/CoSi₂ Schottky barrier is also quite high. As can be derived from XRD data, pure cobalt precipitates are present in silicidized SiGe:Co; however, their presence also ensures the formation of a sufficiently high Schottky barrier of ~600 meV [88]. It is likely that germanium precipitates do not contribute significantly to energy filtering since they are present in both reference SiGe and silicidized samples, but thermal EMF of reference SiGe is not largely different from the known literature data for SiGe alloys without Ge precipitates.

4.6. Power factor measurements

Despite the fact that the electrical conductivity of silicidized SiGe:Co is smaller than that of reference SiGe (Fig. 10, a), its thermal EMF is significantly higher (Fig. 10, b). At this stage of research, we cannot guarantee that electrical measurement results correspond to the characteristics of the alloy specifically, especially when it comes to electrical conductivity. If an electric current was to flow into the substrate during resistivity measurements, the recorded electrical conductivity would be overestimated, though the evaluations presented above indicate that this effect is negligible.

In terms of Seebeck coefficient measurements, the highly conductive substrate can shunt the film's thermal EMF, resulting in measurements being underestimates. Given that the expression used for determining the power factor includes these values in the first and second powers, we can speculate that they are also not too far from their true values. The obtained power factor value for reference SiGe (1 mWm⁻¹K⁻¹ at room temperature) is in good agreement with results found in literature [89].

4.7. Figure of merit measurements

The data presented in Fig. 10, d are obtained for the thermal conductivity of the film in the transverse direction. However, it can be used in combination with electrical conductivity and Seebeck coefficient measured along the film to estimate ZT , since in our samples the characteristic phonon free path lengths are significantly smaller than the layer thickness. In turn, as seen in the cross sections of reference SiGe and SiGe:Co films (Fig. 6), the films' structure is homogeneous, so anisotropy of thermal conductivity is not expected to be present. Therefore, the well-developed structure of the film/substrate interface and the rough surface of films themselves will contribute to additional heat flux dissipation, and the result of ZT calculation would be a slight underestimation.

As has been shown in various theoretical works, a composite material cannot possess a ZT value higher than that of any of its components [90], and the maximum power factor values are exhibited by composites consisting of a metal and a good thermoelectric material [28,29]. However, without taking into account the interface phenomena, their ZT does not exceed that of the thermoelectric material. In [22] this concept was further developed for nanocomposites made of silicide nanoparticles in SiGe alloys, and was experimentally confirmed in [23,91].

In this particular case, the highest achieved ZT is exhibited by silicide SiGe:Co and amounts to a value of 0.72 at 450 K.

5. Conclusions

As part of this work, we have demonstrated a simple method of forming a promising thermoelectric material consisting of a SiGe with CoSi_2 precipitates exhibiting metallic properties. The formation of such a composite is thermodynamically favorable, and it should remain stable when employed in thermoelectric converters.

The structure decorated with preliminarily formed cobalt disilicide precipitates demonstrated good thermoelectric properties at temperatures up to 450 K, which is attributed to the potential barrier at the SiGe/ CoSi_2 heterojunction providing a high thermal EMF due to the charge carrier energy filtering effect. The similarity between crystal lattices at the SiGe/ CoSi_2 interface turned out to be a favorable factor, as the defects arising there make a small contribution to electrical conductivity while also providing efficient scattering of high-frequency phonons. The sizes of these scattering regions provide "hierarchical" scattering, starting from atomic-size defects of the crystal lattice to nanoscale and submicrometer-size grain boundaries, which ensures a decrease in thermal conductivity by reducing lattice thermal conductivity.

It's important to note that the proposed method of thermoelectric material fabrication can be easily integrated into traditional silicon technology in order to create high-efficiency on-chip thermoelectric generators or coolers. Notably, researchers generally try to avoid or minimize the influence of the substrate on the thermoelectric material formed thereon. In our case the obtained ZT values are determined from the "effective" electrical parameters, but perform at a level comparable to the best modern thermoelectric materials of its class throughout the studied temperature range [92].

Funding

This research was financially supported by the Russian Science Foundation (project № 20–19–00720, <https://rscf.ru/project/20–19–00720/>).

CRediT authorship contribution statement

Nikita Grevtsov: Writing – original draft, Methodology, Investigation, Formal analysis. **Eugene Chubenko:** Writing – original draft, Validation, Supervision, Data curation. **Vitaly Bondarenko:** Writing – review & editing, Supervision, Project administration, Formal analysis,

Data curation. **Ilya Gavrilin:** Writing – review & editing, Resources, Investigation, Funding acquisition. **Alexey Dronov:** Resources, Conceptualization. **Sergey Gavrilov:** Resources, Conceptualization. **Dmitry Goroshko:** Writing – review & editing, Resources, Investigation, Data curation. **Olga Goroshko:** Resources, Investigation. **Grigory Rymiski:** Software, Investigation. **Kazimir Yanushkevich:** Software, Resources.

Declaration of competing interest

The authors declare that they have no known competing financial interests or personal relationships that could have appeared to influence the work reported in this paper.

Supplementary materials

Supplementary material associated with this article can be found, in the online version, at [doi:10.1016/j.materresbull.2024.113258](https://doi.org/10.1016/j.materresbull.2024.113258).

Data availability

Data will be made available on request.

References

- [1] A. Henry, R. Prasher, A. Majumdar, Five thermal energy grand challenges for decarbonization, *Nat. Energy* 5 (2020) 635–637, <https://doi.org/10.1038/s41560-020-0675-9>.
- [2] M. d'Angelo, C. Galassi, N. Lecis, Thermoelectric materials and applications: a review, *Energies* (Basel) 16 (2023) 6409, <https://doi.org/10.3390/en16176409>.
- [3] M. Feng, S. Lv, J. Deng, Y. Guo, Y. Wu, G. Shi, M. Zhang, An overview of environmental energy harvesting by thermoelectric generators, *Renew. Sustain. Energy Rev.* 187 (2023) 113723, <https://doi.org/10.1016/j.rser.2023.113723>.
- [4] O. Caballero-Calero, J.R. Ares, M. Martín-González, Environmentally friendly thermoelectric materials: high performance from inorganic components with low toxicity and abundance in the earth, *Adv. Sustain. Syst.* 5 (2021) 2100095, <https://doi.org/10.1002/adsu.202100095>.
- [5] Y. Huang, Z. Yang, Y.-C. Tseng, E. Smith, Y. Mozharivskiy, Unusual role of ZnO nanoparticles in enhancing the thermoelectric performance of GeTe, *J. Alloys. Compd.* 963 (2023) 171136, <https://doi.org/10.1016/j.jallcom.2023.171136>.
- [6] B. Cook, Silicon–Germanium: the legacy lives on, *Energies* (Basel) 15 (2022) 2957, <https://doi.org/10.3390/en15082957>.
- [7] X. Zhang, L.-D. Zhao, Thermoelectric materials: energy conversion between heat and electricity, *J. Materiomics* 1 (2015) 92–105, <https://doi.org/10.1016/j.jmat.2015.01.001>.
- [8] N.M. Ravindra, B. Jariwala, A. Bañobre, A. Maske, *Thermoelectrics: Fundamentals, Materials Selection, Properties, and Performance*, Springer International Publishing, Cham, 2019, <https://doi.org/10.1007/978-3-319-96341-9>.
- [9] D.M. Rowe (Ed.), *Thermoelectrics Handbook*, CRC Press, 2018, <https://doi.org/10.1201/9781420038903>.
- [10] P. Chiang, S. Hu, W.-T. Yen, H.-J. Wu, H.-P. Hsu, C. Lan, A study of iron-doped SiGe growth for thermoelectric applications, *J. Alloys. Compd.* 967 (2023) 171700, <https://doi.org/10.1016/j.jallcom.2023.171700>.
- [11] J. Feng, J. Li, R. Liu, Low-temperature thermoelectric materials and applications, *Nano Energy* 126 (2024) 109651, <https://doi.org/10.1016/j.nanoen.2024.109651>.
- [12] F.D. Rosi, Thermoelectricity and thermoelectric power generation, *Solid. State Electron.* 11 (1968) 833–868, [https://doi.org/10.1016/0038-1101\(68\)90104-4](https://doi.org/10.1016/0038-1101(68)90104-4).
- [13] J.A. Perez-Taborda, M. Muñoz Rojo, J. Maiz, N. Neophytou, M. Martín-González, Ultra-low thermal conductivities in large-area Si-Ge nanomeshes for thermoelectric applications, *Sci. Rep.* 6 (2016) 32778, <https://doi.org/10.1038/srep32778>.
- [14] D.M. Rowe (Ed.), *CRC Handbook of Thermoelectrics*, CRC Press, Boca Raton, FL, 1995.
- [15] Q. Xu, J. Zhou, T.-H. Liu, G. Chen, Effect of electron-phonon interaction on lattice thermal conductivity of SiGe alloys, *Appl. Phys. Lett.* 115 (2019) 023903, <https://doi.org/10.1063/1.5108836>.
- [16] L. Mirizzi, M. Carnevale, M. D'Arienzo, C. Milanese, B. Di Credico, S. Mostoni, R. Scotti, Tailoring the thermal conductivity of rubber nanocomposites by inorganic systems: opportunities and challenges for their application in tires formulation, *Molecules* 26 (2021) 3555, <https://doi.org/10.3390/molecules26123555>.
- [17] B. Liao, B. Qiu, J. Zhou, S. Huberman, K. Esfarjani, G. Chen, Significant reduction of lattice thermal conductivity by the electron-phonon interaction in silicon with high carrier concentrations: a first-principles study, *Phys. Rev. Lett.* 114 (2015) 115901, <https://doi.org/10.1103/PhysRevLett.114.115901>.
- [18] J.A. Pérez-Taborda, O. Caballero-Calero, M. Martín-González, Silicon-Germanium (SiGe) nanostructures for thermoelectric devices: recent advances and new approaches to high thermoelectric efficiency, in: V.I. Talanin (Ed.), *New Research*

- on Silicon - Structure, Properties, Technology, InTech, 2017. <https://doi.org/10.5772/67730>.
- [19] K. Biswas, J. He, I.D. Blum, C.-I. Wu, T.P. Hogan, D.N. Seidman, V.P. Dravid, M. G. Kanatzidis, High-performance bulk thermoelectrics with all-scale hierarchical architectures, *Nature* 489 (2012) 414–418, <https://doi.org/10.1038/nature11439>.
- [20] S.V. Faleev, F. Léonard, Theory of enhancement of thermoelectric properties of materials with nano-inclusions, *Phys. Rev. B* 77 (2008) 214304, <https://doi.org/10.1103/PhysRevB.77.214304>.
- [21] C. Bera, M. Soulier, C. Navone, G. Roux, J. Simon, S. Volz, N. Mingo, Thermoelectric properties of nanostructured Si_{1-x}Ge_x and potential for further improvement, *J. Appl. Phys.* 108 (2010) 124306, <https://doi.org/10.1063/1.3518579>.
- [22] N. Mingo, D. Hauser, N.P. Kobayashi, M. Plissonnier, A. Shakouri, Nanoparticle-in-Alloy Approach to Efficient Thermoelectrics: Silicides in SiGe, *Nano Lett.* 9 (2009) 7111–7115, <https://doi.org/10.1021/nl8031982>.
- [23] A. Nozariasmarz, P. Roy, Z. Zamanipour, J.H. Dycus, M.J. Cabral, J.M. LeBeau, J. S. Krasinski, D. Vashaev, Comparison of thermoelectric properties of nanostructured Mg₂Si, FeSi₂, SiGe, and nanocomposites of SiGe–Mg₂Si, SiGe–FeSi₂, *APL Mater.* 4 (2016) 104814, <https://doi.org/10.1063/1.4966138>.
- [24] A.T. Burkow, Silicide thermoelectrics: materials for energy harvesting, *Physica Status Solidi(a)* 215 (2018) 1800105, <https://doi.org/10.1002/pssa.201800105>.
- [25] Z. Zamanipour, D. Vashaev, Comparison of thermoelectric properties of p-type nanostructured bulk Si_{0.8}Ge_{0.2} alloy with Si_{0.8}Ge_{0.2} composites embedded with CrSi₂ nano-inclusions, *J. Appl. Phys.* 112 (2012) 093714, <https://doi.org/10.1063/1.4764919>.
- [26] K. Favier, G. Bernard-Granger, C. Navone, M. Soulier, M. Boidot, J. Leforestier, J. Simon, J.-C. Tedenac, D. Ravot, Influence of in situ formed MoSi₂ inclusions on the thermoelectrical properties of an N-type silicon–germanium alloy, *Acta Mater.* 64 (2014) 429–442, <https://doi.org/10.1016/j.actamat.2013.10.062>.
- [27] F.W. Dynys, A. Sayir, J. Mackey, A. Sehirlioglu, Thermoelectric properties of WSi₂–SixGe_{1-x} composites, *J. Alloys. Compd.* 604 (2014) 196–203, <https://doi.org/10.1016/j.jallcom.2014.03.133>.
- [28] D.J. Bergman, L.G. Fel, Enhancement of thermoelectric power factor in composite thermoelectrics, *J. Appl. Phys.* 85 (1999) 8205–8216, <https://doi.org/10.1063/1.370660>.
- [29] A. Riss, F. Garmroudi, M. Parzer, A. Pustogow, T. Mori, E. Bauer, Thermoelectric power factor of composites, *Phys. Rev. Appl.* 21 (2024) 014002, <https://doi.org/10.1103/PhysRevApplied.21.014002>.
- [30] S. Ahmad, A. Singh, A. Bohra, R. Basu, S. Bhattacharya, R. Bhatt, K.N. Meshram, M. Roy, S.K. Sarkar, Y. Hayakawa, A.K. Debnath, D.K. Aswal, S.K. Gupta, Boosting thermoelectric performance of p-type SiGe alloys through in-situ metallic YSi₂ nano-inclusions, *Nano Energy* 27 (2016) 282–297, <https://doi.org/10.1016/j.nanoen.2016.07.002>.
- [31] J. Xie, Y. Ohishi, S. Ichikawa, H. Muta, K. Kurosaki, S. Yamanaka, Thermoelectric properties of Si/CoSi₂ sub-micrometer composites prepared by melt-spinning technique, *J. Appl. Phys.* 121 (2017) 205107, <https://doi.org/10.1063/1.4983776>.
- [32] D.O. Shin, M.R. Sardela, S.H. Ban, N.-E. Lee, K.-H. Shim, Strain relaxation of epitaxial CoSi₂ and SiGe layers in cap-Si/Si_{0.83}Ge_{0.17}/Si(0 0 1) and epi-CoSi₂/Si_{0.83}Ge_{0.17}/Si(0 0 1) structures, *Appl. Surf. Sci.* 237 (2004) 139–145, <https://doi.org/10.1016/j.apsusc.2004.06.118>.
- [33] Y. Zeng, H. Li, Y. Du, Y. Pan, Y. Peng, P. Zhou, M. Premovic, Experimental investigation of the Co-Ge phase diagram, *J. Phase Equilib. Diffus.* 38 (2017) 843–852, <https://doi.org/10.1007/s11669-017-0592-1>.
- [34] R. Pretorius, C.C. Theron, A. Vantomme, J.W. Mayer, Compound phase formation in thin film structures, *Crit. Rev. Solid State Mater. Sci.* 24 (1999) 1–62, <https://doi.org/10.1080/10408439991329161>.
- [35] C. Detavernier, T.R.L. Van Meirhaeghe, F. Cardon, K. Maex, CoSi₂ nucleation in the presence of Ge, *Thin. Solid. Films.* 384 (2001) 243–250, [https://doi.org/10.1016/S0040-6090\(00\)01872-1](https://doi.org/10.1016/S0040-6090(00)01872-1).
- [36] S. Lazarouk, V. Bondarenko, P. Pershukovich, S. La Monica, G. Maiello, A. Ferrari, Visible electroluminescence from Al-porous silicon reverse bias diodes formed on the base of degenerate N-type silicon, *MRS Proc.* 358 (1994) 659, <https://doi.org/10.1557/PROC-358-659>.
- [37] N. Vorozov, L. Dolgyi, V. Yakovtseva, V. Bondarenko, M. Balucani, G. Lamedica, A. Ferrari, G. Vitrant, J.E. Broquin, T.M. Benson, H.F. Arrand, P. Sewell, Self-aligned oxidised porous silicon optical waveguides with reduced loss, *Electron. Lett.* 36 (2000) 722, <https://doi.org/10.1049/el:20000490>.
- [38] M. Balucani, P. Nenzi, E. Chubenko, A. Klyshko, V. Bondarenko, Electrochemical and hydrothermal deposition of ZnO on silicon: from continuous films to nanocrystals, *J. NanoPart Res.* 13 (2011) 5985–5997, <https://doi.org/10.1007/s11051-011-0346-7>.
- [39] C. Cirillo, M. Trezza, F. Chiarella, A. Vecchione, V.P. Bondarenko, S.L. Prischepa, C. Attanasio, Quantum phase slips in superconducting Nb nanowire networks deposited on self-assembled Si templates, *Appl. Phys. Lett.* 101 (2012) 172601, <https://doi.org/10.1063/1.4764066>.
- [40] I.M. Gavrillin, N.L. Grevtsov, A.V. Pavlikov, A.A. Dronov, E.B. Chubenko, V. P. Bondarenko, S.A. Gavrilov, A new approach for producing of film structures based on Si_{1-x}Ge_x, *Mater. Lett.* 313 (2022) 131802, <https://doi.org/10.1016/j.matlet.2022.131802>.
- [41] E.B. Chubenko, S.V. Redko, A.I. Sherstnyov, V.A. Petrovich, D.A. Kotov, V. P. Bondarenko, Influence of the surface layer on the electrochemical deposition of metals and semiconductors into mesoporous silicon, *Semiconductors* 50 (2016) 372–376, <https://doi.org/10.1134/S1063782616030040>.
- [42] A.R. Chelyadinsky, A.M. Dorofeev, N.M. Kazuchits, S. La Monica, S.K. Lazarouk, G. Maiello, G. Masini, N.M. Penina, V.F. Stelmakh, V.P. Bondarenko, A. Ferrari, Deformation of porous silicon lattice caused by absorption/desorption processes, *J. Electrochem. Soc.* 144 (1997) 1463–1468, <https://doi.org/10.1149/1.1837612>.
- [43] H. Bandarenka, S.L. Prischepa, R. Fittipaldi, A. Vecchione, P. Nenzi, M. Balucani, V. Bondarenko, Comparative study of initial stages of copper immersion deposition on bulk and porous silicon, *Nanoscale Res. Lett.* 8 (2013) 85, <https://doi.org/10.1186/1556-276X-8-85>.
- [44] D.L. Goroshko, I.M. Gavrillin, S.V. Chusovitina, A.A. Dronov, R.L. Volkov, A. V. Gerasimenko, N.I. Borgardt, S.A. Gavrilov, Electrochemically deposited germanium nanowires: structure and resistivity against high-temperature oxidation, *Appl. Surf. Sci.* 655 (2024) 159677, <https://doi.org/10.1016/j.apsusc.2024.159677>.
- [45] A. Pavlikov, A. Sharafutdinova, I. Gavrillin, V. Zaytsev, A. Dronov, S. Gavrilov, Heat treatment effect on structural and optical properties of germanium nanowires obtained by electrochemical deposition, *Physica Status Solidi(a)* 218 (2021) 2100245, <https://doi.org/10.1002/pssa.202100245>.
- [46] A.V. Pavlikov, P.A. Forsh, P.K. Kashkarov, S.A. Gavrilov, A.A. Dronov, I. M. Gavrillin, R.L. Volkov, N.I. Borgardt, S.N. Bokova-Sirosh, E.D. Obraztsova, Investigation of the Stokes to anti-Stokes ratio for germanium nanowires obtained by electrochemical deposition, *J. Raman Spectrosc.* 51 (2020) 596–601, <https://doi.org/10.1002/jrs.5834>.
- [47] Q. Cheek, Understanding nucleation and growth of crystalline germanium through in-situ studies of the ec-LLS technique, (2021). <https://doi.org/10.7302/2938>.
- [48] F.M. d’Heurle, C.S. Petersson, Formation of thin films of CoSi₂: nucleation and diffusion mechanisms, *Thin. Solid. Films.* 128 (1985) 283–297, [https://doi.org/10.1016/0040-6090\(85\)90080-X](https://doi.org/10.1016/0040-6090(85)90080-X).
- [49] F. Zeng, X. Xiong, B. Huang, Cobalt silicide formations and magnetic properties of laser ablated Co(Cr) thin films, *Intermetallics* (Barking) 18 (2010) 306–311, <https://doi.org/10.1016/j.intermet.2009.07.027>.
- [50] J. Chivot, L. Mendoza, C. Mansour, T. Pauporté, M. Cassir, New insight in the behaviour of Co–H₂O system at 25–150°C, based on revised Pourbaix diagrams, *Corros. Sci.* 50 (2008) 62–69, <https://doi.org/10.1016/j.corsci.2007.07.002>.
- [51] K. Barla, R. Herino, G. Bomchil, J.C. Pfister, A. Freund, Determination of lattice parameter and elastic properties of porous silicon by X-ray diffraction, *J. Cryst. Growth* 68 (1984) 727–732, [https://doi.org/10.1016/0022-0248\(84\)90111-8](https://doi.org/10.1016/0022-0248(84)90111-8).
- [52] N. Grevtsov, E. Chubenko, V. Bondarenko, I. Gavrillin, A. Dronov, S. Gavrilov, G. Rymys, K. Yanushkevich, D. Goroshko, E. Argunov, Composition-adjustable silicon-germanium alloy films based on porous silicon matrices, *Mater. Today Commun.* 38 (2024) 107886, <https://doi.org/10.1016/j.mtcomm.2023.107886>.
- [53] H. Aharoni, 13. Measurement of the lattice constant of Si Ge heteroepitaxial layers grown on a silicon substrate, *Vacuum* 28 (1978) 571–578, [https://doi.org/10.1016/0042-207X\(78\)90014-3](https://doi.org/10.1016/0042-207X(78)90014-3).
- [54] L. Vegard, Die Konstitution der Mischkristalle und die Raumfüllung der Atome, *Z. Physik* 5 (1921) 17–26, <https://doi.org/10.1007/BF01349680>.
- [55] J.P. Dismukes, L. Ekstrom, E.F. Steigmeier, I. Kudman, D.S. Beers, Thermal and electrical properties of heavily doped Ge-Si alloys up to 1300°K, *J. Appl. Phys.* 35 (1964) 2899–2907, <https://doi.org/10.1063/1.1713126>.
- [56] J. Humlíček, M. Garriga, M.L. Alonso, M. Cardona, Optical spectra of Si x Ge_{1-x} alloys, *J. Appl. Phys.* 65 (1989) 2827–2832, <https://doi.org/10.1063/1.342720>.
- [57] D. Rouchon, M. Mermoux, F. Bertin, J.M. Hartmann, Germanium content and strain in Si_{1-x}Ge_x alloys characterized by Raman spectroscopy, *J. Cryst. Growth* 392 (2014) 66–73, <https://doi.org/10.1016/j.jcrysgro.2014.01.019>.
- [58] S. Sugawa, R. Yokogawa, K. Yoshioka, Y. Arai, I. Yonenaga, A. Ogura, Temperature dependence of Raman peak shift in single-crystalline silicon-germanium, *ECS J. Solid State Sci. Technol.* 12 (2023) 064004, <https://doi.org/10.1149/2162-8777/acdfia>.
- [59] V.I. Korepanov, D.M. Sedlovets, An asymmetric fitting function for condensed-phase Raman spectroscopy, *Analyst* 143 (2018) 2674–2679, <https://doi.org/10.1039/C8AN00710A>.
- [60] Y. Gao, P. Yin, Origin of asymmetric broadening of Raman peak profiles in Si nanocrystals, *Sci. Rep.* 7 (2017) 43602, <https://doi.org/10.1038/srep43602>.
- [61] J.H. Parker, D.W. Feldman, M. Ashkin, Raman scattering by silicon and germanium, *Phys. Rev.* 155 (1967) 712–714, <https://doi.org/10.1103/PhysRev.155.712>.
- [62] C.-W. Tang, C.-B. Wang, S.-H. Chien, Characterization of cobalt oxides studied by FT-IR, Raman, TPR and TG-MS, *Thermochim. Acta* 473 (2008) 68–73, <https://doi.org/10.1016/j.tca.2008.04.015>.
- [63] H.G. Tompkins, J.A. Augis, The oxidation of cobalt in air from room temperature to 467°C, *Oxid. Met.* 16 (1981) 355–369, <https://doi.org/10.1007/BF00611349>.
- [64] M.L. Alonso, K. Winer, Raman spectra of c - Si 1 - x Ge x alloys, *Phys. Rev. B* 39 (1989) 10056–10062, <https://doi.org/10.1103/PhysRevB.39.10056>.
- [65] P.M. Mooney, F.H. Dacol, J.C. Tsang, J.O. Chu, Raman scattering analysis of relaxed Ge x Si_{1-x} alloy layers, *Appl. Phys. Lett.* 62 (1993) 2069–2071, <https://doi.org/10.1063/1.109481>.
- [66] J.C. Tsang, P.M. Mooney, F. Dacol, J.O. Chu, Measurements of alloy composition and strain in thin Ge x Si_{1-x} layers, *J. Appl. Phys.* 75 (1994) 8098–8108, <https://doi.org/10.1063/1.356554>.
- [67] V.A. Volodin, M.D. Efreimov, A.S. Deryabin, L.V. Sokolov, Determination of the composition and stresses in GeSi(1-x) heterostructures from Raman spectroscopy data: refinement of model parameters, *Semiconductors* 40 (2006) 1314–1320, <https://doi.org/10.1134/S106378260611011X>.
- [68] L.A.K. Staveley, *The Characterization of Chemical Purity: Organic Compounds, Elsevier Science, Kent, 2016*.
- [69] C.K. Glassbrenner, G.A. Slack, Thermal conductivity of silicon and germanium from 3°K to the melting point, *Phys. Rev.* 134 (1964) A1058–A1069, <https://doi.org/10.1103/PhysRev.134.A1058>.

- [70] D.L. Goroshko, I.M. Gavrilin, A.A. Dronov, O.A. Goroshko, L.S. Volkova, N. L. Grevtsov, E.B. Chubenko, V.P. Bondarenko, Electrical transport in porous structures of Si-Ge/c-Si formed by the electrochemical deposition of germanium in porous silicon, *Semiconductors* 57 (2023) 46–51, <https://doi.org/10.1134/S1063782623010104>.
- [71] C.K. Maiti, L.K. Bera, S. Chattopadhyay, Strained-Si heterostructure field effect transistors, *Semicond. Sci. Technol.* 13 (1998) 1225–1246, <https://doi.org/10.1088/0268-1242/13/11/002>.
- [72] R. Basu, A review on single crystal and thin film Si-Ge alloy: growth and applications, *Mater. Adv.* 3 (2022) 4489–4513, <https://doi.org/10.1039/D2MA00104G>.
- [73] R.T. Tung, Schottky barrier heights of single crystal silicides on Si(111), *J. Vacuum Sci. Technol. B* 2 (1984) 465–470, <https://doi.org/10.1116/1.582896>.
- [74] K. Ishida, T. Nishizawa, M.E. Schlesinger, The Co-Si (Cobalt-Silicon) system, *JPE* 12 (1991) 578–586, <https://doi.org/10.1007/BF02645074>.
- [75] D.G. Cahill, Analysis of heat flow in layered structures for time-domain thermoreflectance, *Rev. Sci. Instrum.* 75 (2004) 5119–5122, <https://doi.org/10.1063/1.1819431>.
- [76] C. Dames, Measuring the thermal conductivity of thin films: 3 omega and related electrochemical methods, *Ann. Rev. Heat Transf.* 16 (2013) 7–49, <https://doi.org/10.1615/AnnualRevHeatTransfer.v16.20>.
- [77] S.A. Mala, L. Tsybeskov, D.J. Lockwood, X. Wu, J.-M. Baribeau, Raman scattering in Si/SiGe nanostructures: revealing chemical composition, strain, intermixing, and heat dissipation, *J. Appl. Phys.* 116 (2014) 014305, <https://doi.org/10.1063/1.4886598>.
- [78] D.L. Goroshko, I.M. Gavrilin, A.A. Dronov, O.A. Goroshko, L.S. Volkova, Structure and thermal conductivity of thin films of the Si_{1-x}Ge_x alloy formed by electrochemical deposition of germanium into porous silicon, *Optoelectron. Instrument. Proc.* 59 (2023) 727–734, <https://doi.org/10.3103/S8756699023060043>.
- [79] F. Cerdeira, M.I. Alonso, D. Niles, M. Garriga, M. Cardona, E. Kasper, H. Kibbel, Resonant Raman scattering in short-period (Si)_n/(Ge)_m superlattices, *Phys. Rev. B* 40 (1989) 1361–1364, <https://doi.org/10.1103/PhysRevB.40.1361>.
- [80] Y. Hu, L. Zeng, A.J. Minnich, M.S. Dresselhaus, G. Chen, Spectral mapping of thermal conductivity through nanoscale ballistic transport, *Nat. Nanotech* 10 (2015) 701–706, <https://doi.org/10.1038/nnano.2015.109>.
- [81] I. Yonenaga, T. Akashi, T. Goto, Thermal and electrical properties of Czochralski grown GeSi single crystals, *J. Phys. Chem. Solids* 62 (2001) 1313–1317, [https://doi.org/10.1016/S0022-3697\(01\)00026-9](https://doi.org/10.1016/S0022-3697(01)00026-9).
- [82] C.B. Vining, W. Laskow, J.O. Hanson, R.R. Van Der Beck, P.D. Gorsuch, Thermoelectric properties of pressure-sintered Si_{0.8}Ge_{0.2} thermoelectric alloys, *J. Appl. Phys.* 69 (1991) 4333–4340, <https://doi.org/10.1063/1.348408>.
- [83] R. Cheaito, J.C. Duda, T.E. Beechem, K. Hattar, J.F. Ihlefeld, D.L. Medlin, M. A. Rodriguez, M.J. Campion, E.S. Piekos, P.E. Hopkins, Experimental investigation of size effects on the thermal conductivity of silicon-germanium alloy thin films, *Phys. Rev. Lett.* 109 (2012) 195901, <https://doi.org/10.1103/PhysRevLett.109.195901>.
- [84] S.M. Sze, K.K. Ng, *Physics of Semiconductor Devices*, Wiley-Interscience, Hoboken, NJ, 2007. Third edition.
- [85] E. Bucher, S. Schulz, M.Ch. Lux-Steiner, P. Munz, U. Gubler, F. Greuter, Work function and barrier heights of transition metal silicides, *Appl. Phys. A* 40 (1986) 71–77, <https://doi.org/10.1007/BF00616480>.
- [86] J.P. Heremans, V. Jovovic, E.S. Toberer, A. Saramat, K. Kurosaki, A. Charoenphakdee, S. Yamanaka, G.J. Snyder, Enhancement of thermoelectric efficiency in PbTe by distortion of the electronic density of states, *Science* (1979) 321 (2008) 554–557, <https://doi.org/10.1126/science.1159725>.
- [87] M. Amato, M. Bertocchi, S. Ossicini, Work function bowing in Si_{1-x}Ge_x heterostructures: *Ab initio* results, *J. Appl. Phys.* 119 (2016) 085705, <https://doi.org/10.1063/1.4942526>.
- [88] S. Adachi, *Properties of Semiconductor alloys: group-IV, III-V and II-VI semiconductors*, Corrections made August 2012, Wiley, a John Wiley & Sons, Ltd, Publication, Chichester, 2012.
- [89] R. Basu, S. Bhattacharya, R. Bhatt, M. Roy, S. Ahmad, A. Singh, M. Navaneethan, Y. Hayakawa, D.K. Aswal, S.K. Gupta, Improved thermoelectric performance of hot pressed nanostructured n-type SiGe bulk alloys, *J. Mater. Chem. A* 2 (2014) 6922, <https://doi.org/10.1039/c3ta14259k>.
- [90] D.J. Bergman, O. Levy, Thermoelectric properties of a composite medium, *J. Appl. Phys.* 70 (1991) 6821–6833, <https://doi.org/10.1063/1.349830>.
- [91] A. Nozariasbmarz, Z. Zamanipour, P. Norouzzadeh, J.S. Krasinski, D. Vashaee, Enhanced thermoelectric performance in a metal/semiconductor nanocomposite of iron silicide/silicon germanium, *RSC. Adv.* 6 (2016) 49643–49650, <https://doi.org/10.1039/C6RA01947A>.
- [92] A. Nozariasbmarz, A. Agarwal, Z.A. Coutant, M.J. Hall, J. Liu, R. Liu, A. Malhotra, P. Norouzzadeh, M.C. Öztürk, V.P. Ramesh, Y. Sargolzaeiaval, F. Suarez, D. Vashaee, Thermoelectric silicides: a review, *Jpn. J. Appl. Phys.* 56 (2017), <https://doi.org/10.7567/JJAP.56.05DA04>, 05DA04.